TEL AVIV UNIVERSITY

The Iby and Aladar Fleischman Faculty of Engineering
The Zandman-Slaner School of Graduate Studies

UNIVERSAL ALGORITHM TO PREDICT CLEAVAGE PLANES IN SINGLE CRYSTALS

Submitted towards the degree of
Master of Science in Materials Science and Engineering
by

Uriel Vaknin

August 2020

TEL AVIV UNIVERSITY

The Iby and Aladar Fleischman Faculty of Engineering
The Zandman-Slaner School of Graduate Studies

UNIVERSAL ALGORITHM TO PREDICT CLEAVAGE PLANES IN SINGLE CRYSTALS

Submitted towards the degree of
Master of Science in Materials Science and Engineering
by

Uriel Vaknin

This research was carried out in the
Department of Materials Science and Engineering
under the supervision of Dr. Semën Gorfman
and Prof. Dov Sherman

August 2020

Acknowledgements

I would first like to express my gratitude to my main thesis advisor Dr. Semën Gorfman, for your committed, professional and uncompromising guidance. Thank you for hundreds of hours in which you taught me practically everything I know about MATLAB and crystallography.

At the same time, I would also like to thank my advisor Prof. Dov Sherman, helping us with the experimental aspect of this work with your enormous knowledge on cleavage and fracture. Thank you for your smart advices and sharp insights.

To Dr. Hyeokmin Choe our Korean friend, for helping me at difficult times when nothing worked on the program. Thank you also for your pleasant presence and attitude.

To Dr. David Spirito our group member, for helping with the program and being with us towards almost the whole process.

To the department of Materials Science and Engineering, for allowing me to perform this M.Sc. thesis work in your department.

Last, I would like to express my sincere gratitude to my mom, which helped me mentally and financially throughout this degree. Thank you for your delicious food!

Abstract

Cleavage describes the tendency of a crystal to break easily along specific crystallographic planes. Acquiring the information about cleavage in a given crystal microstructure is essential for the investigation of key mechanical properties such as fracture toughness, plasticity and strength. Although cleavage planes are commonly known for some simple materials (e.g. (110) and (111) of silicon), such information about any arbitrary crystal is not available. There are no simple computational methods to predict cleavage planes in single crystals, apart from interactive visual inspection of three-dimensional structures using graphical programs (like CrystalMaker or VESTA). Developing such a method may contribute significantly to the understanding of physical and mechanical properties of crystals. It also provides a solid prediction of their cleavage planes, and may open the door to find new ones.

This work aims to develop an algorithm and a computer program for automatic inspection of crystal structures and prediction of its likely cleavage planes. The algorithm enumerates all possible lattice planes, listing their Miller indices, counting the number of intersected atoms for every plane and its position along the related crystallographic direction. We modelled atoms by thermal ellipsoids - probability density functions (PDFs) derived from their atomic displacement parameters (ADPs). Our algorithm was tested on simple inorganic crystal structures such as Si, α-SiO_2 and $LiNbO_3$.

We believe that our algorithm can be used for fast, efficient and intuitive prediction of cleavage planes to be further approved by rigorous and more time-consuming density functional theory calculations.

Contents

Symbols

Big Latin letters

Si	Silicon atom
O	Oxygen atom
Nb	Niobium atom
Li	Lithium atom
U	Potential energy
U_A	Energy of applied loading system
U_E	Elastic strain energy
U_M	Mechanical energy
U_S	Surface free energy of crack area
W_L	External work
E	Young's modulus
E'	E, plane stress; $E/(1-v^2)$, plane strain
$[U_A]$	Orientation matrix
$[U_B]$	Reciprocal orientation matrix
R	Fractional atomic position
N	Natural number
$[G]$	Matrix of dot products
$[G^*]$	Reciprocal matrix of dot products
$[I]$	Identity matrix
$[S]$	Rotation matrix
D	Distance between two points; Atomic density
M	Average atomic density
$\boldsymbol{A_1}, \boldsymbol{A_2}, \boldsymbol{A_3}$	Basis vectors of the transformed unit cell
$\mathbf{B}$	Reciprocal lattice vector

Small Latin letters

a	Half crack length, internal crack; Crack length, edge crack
a_0	Precrack size
b	Minor axes in Inglis elliptical cavity
c	Major axes in Inglis elliptical cavity; Characteristic crack size
d	Interplanar distance
x, y, z	Cartesian coordinates; Fractional atomic positions
$\boldsymbol{a_1}, \boldsymbol{a_2}, \boldsymbol{a_3}$	Basis vectors for a 3D crystal structure
a_1, a_2, a_3	Lattice parameters (lengths)
$\boldsymbol{a_1^*}, \boldsymbol{a_2^*}, \boldsymbol{a_3^*}$	Reciprocal basis vectors
a_1^*, a_2^*, a_3^*	Reciprocal lattice parameters
$\boldsymbol{e_1}, \boldsymbol{e_2}, \boldsymbol{e_3}$	Cartesian axes
$h_1 h_2 h_3$	Miller indices
$\boldsymbol{u}$	3D row vector (1x3)
$\boldsymbol{v}$	3D column vector (3x1)
q, p	Arbitrary points in 3D space
$\boldsymbol{d}$	Displacement vector, 3x1 column vector
r	Electron density position
$u_1, u_2, \ldots, u_N$	Displacement coordinates
x_0, y_0, z_0	Atom's center position

Big Greek letters

Γ_0	Cleavage energy

Small Greek letters

σ	Stress; Standard information obtained by x-ray diffraction
σ_A	Applied uniform stress
σ_C	Stress at tip of elliptical cavity

σ_F	Failure stress
ρ	Tip radius of elliptical cavity
γ	Surface free energy per unit area; Lattice parameter (angle)
$\alpha_1, \alpha_2, \alpha_3$	Lattice parameters (angles)
$\alpha_1^*, \alpha_2^*, \alpha_3^*$	Reciprocal lattice parameters
$\langle\rho(r)\rangle$	Time average electron density
ρ_{RG}	Rigid group density
ρ_S	Static density
$\langle\rho_{atom}(r)\rangle$	Time average electron density of an atom
δ	Kronecker delta
β^{jk}	Anisotropic displacement parameters

Abbreviations

DFT	Density functional theory
α-SiO_2	α-Quartz
$LiNbO_3$	Lithium Niobate
NPD	Nuclear probability distribution
PDF	Probability density function
$ADPs$	Atomic displacement parameters
AAD	Average atomic density
CA	Cleaving ability
CE	Cleavage energy
CIF	Crystallographic information file

Table of figures

Table of tables

1 Introduction

Although the surface free energy of a solid is one of its most fundamental materials properties, there is a lack of experimentally measured values for it. Surface free energy is due to more than one dangling bond which makes the free surface energy higher than the bulk. Cleavage experiments are possible direct way to measure it (in ideally brittle materials). The mechanical energy required to cause cleavage (under thermodynamic equilibrium) per unit area equals to twice the intrinsic surface energy. If the cleavage is carried out in an irreversible fashion, the mechanical energy increases and is greater than the intrinsic surface energy than the crack will initiate[1] (Griffith). Cleavage planes are commonly known for some simple materials (e.g. (110) and (111) for silicon)[2,3].

Data of fracture energy of single crystals is limited because of the difficulties in performing precisely controlled cleavage experiments. There is also a lack of atomic scale simulations allowing for the quantitative comparison with fracture experiments. No simple computational methods are available for prediction of the cleavage planes in single crystals, and most of the simulations available today in this field are based on the more demanding density functional theory (DFT) calculations[4–11]. The main disadvantage of the DFT methods is their complexity and time-consuming nature.

Developing a simpler method of investigating cleavage in single crystals may contribute considerably to the understanding of their mechanical properties. It may also provide a solid prediction of their cleavage planes and open the door to find new ones.

The goal of this work is to develop a new simple approach universal to inspect and predict cleavage planes in crystal structures. The algorithm was tested on simple inorganic crystals such as Si, α-SiO_2 and $LiNbO_3$. For the $LiNbO_3$ crystal structure, the results were confirmed experimentally[12].

2 Research goals

The aim of this work is to develop a universal algorithm and computer program for automatic inspection of crystal structures, and the prediction of its likely cleavage planes. Using this algorithm, we should be able to substitute the manual structure inspection, finding cleavage planes for any single crystal. That includes planes that were not found

experimentally yet. The importance of this work derives from the simplicity of the algorithm and the time it may save.

DFT calculations may give very accurate results but the problems with these calculations are its complexity and the time they consume[6,8,11]. Our program is by far more intuitive than these DFT calculations. The main idea beyond the program is a 3D rotation of the crystal under investigation, looking for the biggest gaps in between planes. These gaps are considered as the least dense planes, and they are potential cleavage planes.

Future work may rely on our algorithm as a strong basis to improve the model, acquiring even better predictions with higher significance.

3 Fracture of brittle materials

Most materials show a tendency to fracture when stressed beyond certain critical level[13–15]. Early in the twentieth century engineers came to the conclusion that strength is a material property[16]. It was shown, theoretically, that the theoretical strength of ideally perfect crystal within the elastic region is directly related to its elastic modulus ($\sigma=E/\pi$). However, the practical strength of these materials is two to four orders of magnitude lower than that strength, presumably due to the presence of defects or flaws in the material. A breakthrough in modeling of strength came in 1920 with the seminal work of Griffith[17]. Griffith considered a crack like defect in a solid subjected to an applied external far field stress, and formulated a criterion for its strength from the fundamental energy balance.

3.1 Inglis elliptical cavity problem

Griffith's study was based on the Inglis' stress analysis in the early 20th century, of an elliptical cavity in a uniformly stressed plate as a boundary value problem of elastic body. Inglis analysis showed that the local stresses at the tip of a sharp notch is several times higher than the applied stress. This mean that even submicroscopic flaws may severely weaken the solids.

Inglis considered an elliptical cavity of semi-axes b and c, in a uniformly stressed plate[16] (Figure 3.1) and formulated the elastic stress and strain fields in the body containing this cavity.

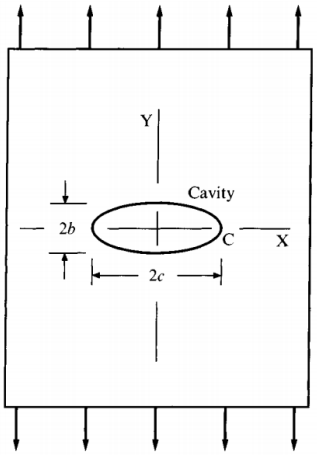

Figure 3.1 Plate containing elliptical cavity with semi-axes b, c;
The plate is subjected to uniform tension $\boldsymbol{\sigma_A}$. C is the notch tip[18]

If we assume that Hooke's law holds everywhere in the plate, the boundary of the hole is stress-free, and that *b* and *c* are small compared to the plate dimensions, though the mathematics involved in this problem is quite complex, there are some amazingly simple results derived from the analysis. We start by writing the equation of the ellipse shown in in Figure 3.1 –

$$\frac{x^2}{c^2} + \frac{y^2}{b^2} = 1 \qquad 3.1$$

The greatest concentration of stress appears at the point C given by[18] –

$$\frac{\sigma_C}{\sigma_A} = 1 + 2\frac{c}{b} \qquad 3.2$$

Where σ_A is an applied uniform stress, and σ_C is the stress at the tip (point C). This ratio on equation 3.2 is known as the elastic stress concentration factor. From this equation it's clear that the stress concentration factor depends more on the shape of the crack (the ratio between c and b), rather than its size.

3.2 Griffith energy-balance concept

In order to model crack initiation Griffith assumed a reversible thermodynamic energy balance. Figure 3.2 describes a system of an infinite linear elastic body having elastic modulus, E, and containing a crack of length 2a at its center. The system is loaded by far field stresses, σ, applied perpendicular to the crack.

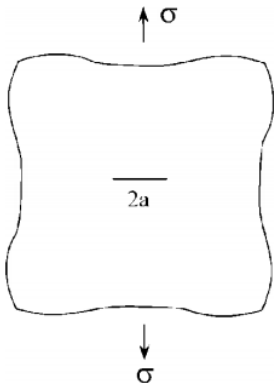

Figure 3.2 Griffith geometrical model;
A plate with a crack 2a subjected to an external sress[18]

Griffith used the above configuration and minimized the energy of the system, where the crack is in an equilibrium state, and thus on the verge of extension. He started with the expression for the total potential energy U of the system. To do this he considered the individual energy terms that are subject to change as the crack is allowed to undergo virtual extension. The system energy associated with crack formation can be divided into mechanical and free surface energies U_M and U_S respectively. The mechanical energy is given by –

$$U_M = -W_L + U_E \qquad 3.3$$

Where W_L is the external work (and therefore negative) of the applied load, and U_E is the internal strain energy stored within the elastic body. The term U_S is the free surface energy of the crack surfaces. The total energy can be written as –

$$U = U_M + U_S \qquad 3.4$$

Thermodynamic equilibrium is achieved by balancing the mechanical and surface energies over a virtual crack extension da (Figure 3.2). The mechanical energy will generally increase as the crack extends, but it is in a negative sign. The Griffith energy-balance concept, a formal statement of which is given by the equilibrium requirement –

$$dU/dc = 0 \qquad 3.5$$

Where dc is a small crack extension. Meaning that a crack would extend or retract reversibly for small displacements whether the term dU/dc is negative or positive.

In order to confirm his theory Griffith needed an elastic model for a crack, where he can calculate the energy according to equation 3.4. For that he used the Inglis analysis, considering an infinitely narrow elliptical cavity (C>>1, b → 0, Figure 3.1) of length 2c in a remote, uniform tensile stress field σ_A. Then, he searched for a well-behaved material, isotropic and closely obeying Hooke's law at all stresses, and glass was selected.

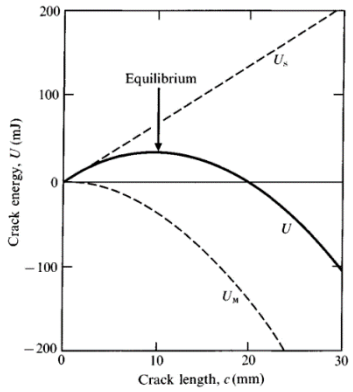

Figure 3.3 Energetics of Griffith crack in uniform tension, plane stress
U_M and U_S are the mechanical and surface energies, respectively. U is the total energy[18]

Griffith used a result from linear elasticity theory that for a body under constant stress during crack formation so we get $U_M = -U_E$. The negative sign indicates a reduction in

$$W_L = 2U_E \qquad 3.6$$

the mechanical energy under crack formation. From the Inglis solution of the stress and strain fields Griffith evaluated the strain energy density to be –

$$U_E = \frac{\pi a^2 \sigma_A^2}{E'} \qquad 3.7$$

Where E' is the Young's modulus that equals E in plane stress (thin plates) and $E/(1-\nu^2)$ in plane strain (thick plates), with ν the Poisson's ratio. The surface energy of the crack system for a unit width is:

$$U_s = 4c\gamma \qquad 3.8$$

with γ being the free surface energy per unit area. The total system energy in this case (equation 3.4) becomes –

$$U(c) = -\frac{\pi c^2 \sigma_A^2}{E'} + 4c\gamma \qquad 3.9$$

In Figure 3.3 we can see the mechanical energy $U_M(c)$, surface energy $U_s(c)$, and total energy. If we apply the Griffith equilibrium condition (3.5) on (3.9) we can calculate the critical conditions at which failure occurs, $\sigma_A < \sigma_F$, $c = c_0$ which is –

$$\sigma_F = \left(\frac{2E'\gamma}{\pi c_0}\right)^{1/2} \qquad 3.10$$

Both Figure 3.3 and the negative value of the second derivative of U(c) imply that the system energy is maximum at equilibrium, meaning the configuration is unstable. Therefore at $\sigma_A < \sigma_F$ the crack remains stationary at size c_0, and at $\sigma_F > \sigma_A$ it propagates spontaneously without limit.

3.3 Cleavage

The way a crystal breaks is determined by the arrangement of its atoms and the strength of its chemical bonds. Cleavage is the tendency of crystalline materials to split along specific crystallographic planes, known as cleavage planes. Crystal lattice planes with low surface energies would be energetically favored as cleavage planes[15].

There are a few different types of cleavage such as Basal or Pinacoidal cleavage, Cubic cleavage and Octahedral cleavage which are differentiating from one another by the space group and symmetry of the crystal, and the number of cleavage planes[19].

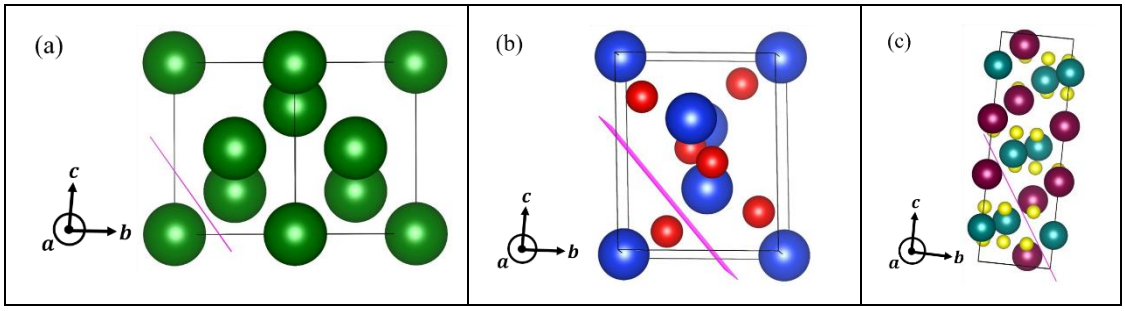

Figure 3.4 Schematic illustration of the cleavage planes for different crystal structures using. The drawings were produced using VESTA program[20];
(a) – (111) cleavage plane in Si, (b) – (011) cleavage plane in α-SiO_2, (c) – (012) cleavage plane in $LiNbO_3$

3.4 Cleavage energy

The energy required to initiate a crack is denotes by Γ_0. This is the lowest value of energy to initiate a slowly propagating crack. Usually the cleavage energy is twice the free surface energy, because two surfaces are exposed in the cleaving process, having the same surface energy[15]

$$\Gamma_0 = 2\gamma \qquad 3.11$$

It is also possible that each of the surfaces exposed in the cleaving process will carry a different surface energy γ_1, γ_2. In this case the cleaving energy would be the sum of the two surface energies[12]

$$\Gamma_0 = \gamma_1 + \gamma_2 \qquad 3.12$$

4 Introduction to Crystallography

4.1 The crystal structure

Crystal is a long-range ordered arrangement of atoms. The most common type of a long-range order is a three-dimensional periodicity. It is possible to define an entire crystal structure by a unit cell and a crystal lattice, so that the unit cell has to be translated into each point of a crystal lattice. It is important to distinguish between crystal lattice and crystal structure. The first one is a mathematical object, which describes the periodicity of the crystal structure, and the second is the convolution of the unit cell and the crystal lattice. Figure 4.1 illustrates the concepts described above. It consists of a motif (c), a lattice (b), and the structure (a). The motif is the “unit cell”, the repeating unit, the lattice is in fact what we call a crystal lattice, and the structure is the combination of the two creating the crystal structure.

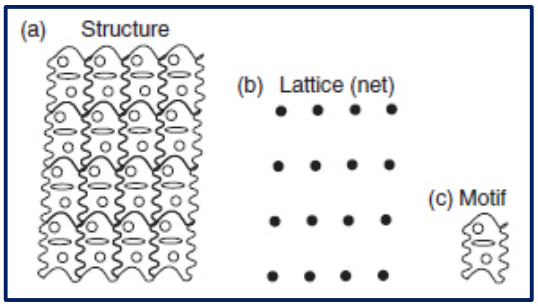

Figure 4.1 Fundamental aspects of crystals;
(a) A periodic pattern (b) 2D net – the lattice (c) Motif – repeating unit[21]

4.1.1 Single crystals

A single crystal is a material in which the crystal lattice is continuous and unbroken to the edges of the sample. Single crystals may have many unique mechanical, optical and electrical properties, depending on the structure and symmetry[22]. In general, physical properties of crystals are anisotropic. Single crystals have many high-technological applications[23–27].

The entropy considerations dictate that any crystal must contain some imperfections in its structure, such as impurities, inhomogeneous strain and dislocations. The opposite of a single crystal is an amorphous structure where the atomic position is limited to short range order only.

4.1.2 Basis vectors and lattice parameters

Basis vectors are three non-coplanar vectors, constructing the frame of the unit cell. Figure 4.2 describes the basis vectors $\boldsymbol{a_1}, \boldsymbol{a_2}, \boldsymbol{a_3}$ for an arbitrary 3D crystal structure. The lattice

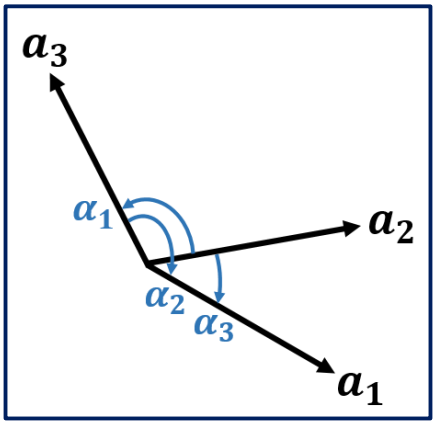

Figure 4.2 Basis vectors and lattice parameters for a 3D crystal structure;
$\boldsymbol{a_1}, \boldsymbol{a_2}, \boldsymbol{a_3}$ are the basis vectors and $\boldsymbol{\alpha_1}, \boldsymbol{\alpha_2}, \boldsymbol{\alpha_3}$ are the angles between them

parameters a_1, a_2, a_3 are therefore the lengths of the basis vectors, and the angles between them are $\alpha_1, \alpha_2, \alpha_3$. α_1 is the angle between $\boldsymbol{a_2}$ and $\boldsymbol{a_3}$, α_2, is the angle between $\boldsymbol{a_1}$ and $\boldsymbol{a_3}$, and α_3 is the angle between $\boldsymbol{a_1}$ and $\boldsymbol{a_2}$, as shown in Figure 4.2.

4.1.3 Reciprocal basis vectors

Reciprocal basis vectors are three non-coplanar vectors, which satisfy the following condition

$$\boldsymbol{a_i a_j}^* = \delta_{ij} \qquad 4.1$$

Where δ_{ij} is the Kronecker delta –

$$\delta_{ij} = \begin{cases} 1 & if \;\; i = j \\ 0 & if \;\; i \neq j \end{cases}$$

Whereas the basis vectors serve us to describe and build the unit cell and the whole lattice, the reciprocal basis vectors have many applications in crystallography and in solid state physics. In the scope of this thesis work, they will help us to determine the indices of lattice planes, and we will talk about it later.

4.1.4 Orientation matrix and reciprocal orientation matrix

The orientation matrix describes how a crystallographic coordinate system is oriented with respect to a fixed Cartesian coordinate system. It is defined as

$$[U_A] = \begin{bmatrix} a_{11} & a_{12} & a_{13} \\ a_{21} & a_{22} & a_{23} \\ a_{31} & a_{32} & a_{33} \end{bmatrix}$$

Where the columns of $[U_A]$; $\boldsymbol{a_1} = \begin{pmatrix} a_{11} \\ a_{21} \\ a_{31} \end{pmatrix}, \boldsymbol{a_2} = \begin{pmatrix} a_{12} \\ a_{22} \\ a_{32} \end{pmatrix}, \boldsymbol{a_3} = \begin{pmatrix} a_{13} \\ a_{23} \\ a_{33} \end{pmatrix}$ are the coordinates of the basis vectors $\boldsymbol{a_1}, \boldsymbol{a_2}, \boldsymbol{a_3}$, with respect to the Cartesian coordinate system. a_{ij} is the projection of $\boldsymbol{a_j}$ on $\boldsymbol{e_i}$ (the Cartesian axis), as shown in Figure 4.3.

The reciprocal orientation matrix describes how the reciprocal crystallographic coordinate system is oriented with respect to the same Cartesian coordinate system. It is defined as

$$[U_B] = \begin{bmatrix} a_{11}^* & a_{12}^* & a_{13}^* \\ a_{21}^* & a_{22}^* & a_{23}^* \\ a_{31}^* & a_{32}^* & a_{33}^* \end{bmatrix}$$

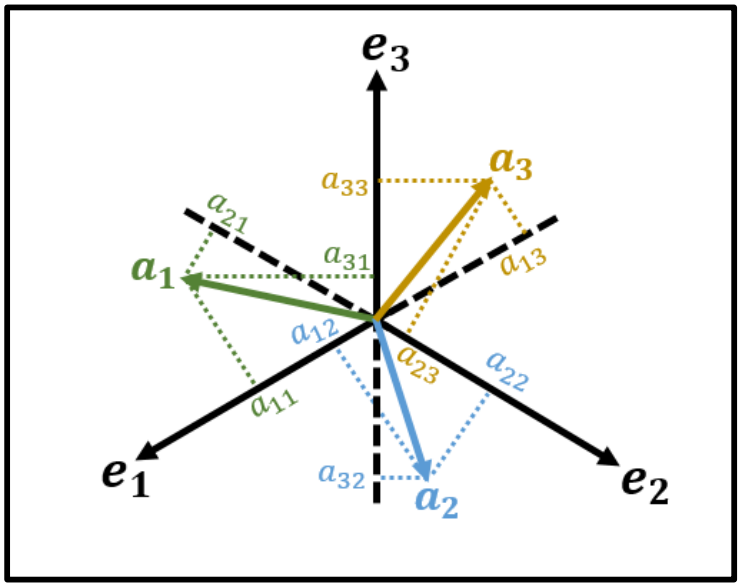

Figure 4.3 Crystallographic vs Cartesian coordinate systems;
Vectors $\boldsymbol{a_1}, \boldsymbol{a_2}, \boldsymbol{a_3}$ are projected onto the Cartesian axes $\boldsymbol{e_1}, \boldsymbol{e_2}, \boldsymbol{e_3}$

Here the columns of $[U_B]$ are the coordinates of the basis vectors $\boldsymbol{a_1^*}, \boldsymbol{a_2^*}, \boldsymbol{a_3^*}$ with respect to the Cartesian coordinate system, as shown in Figure 4.4. The relation between $[U_A]$ and

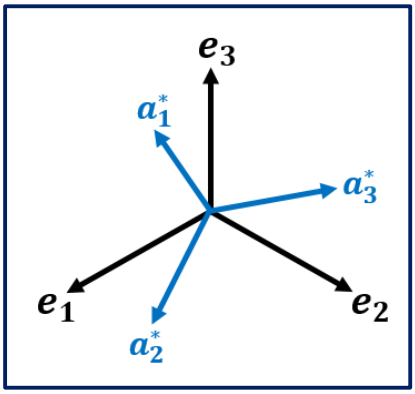

Figure 4.4. Reciprocal crystallographic vs Cartesian coordinate systems;
$\boldsymbol{a_1^*}, \boldsymbol{a_2^*}, \boldsymbol{a_3^*}$ are the reciprocal basis and $\boldsymbol{e_1}, \boldsymbol{e_2}, \boldsymbol{e_3}$ are the Cartesian axes

$[U_B]$ can be obtained by –

$$[U_B^T][U_A] = \begin{bmatrix} a_{11}^* & a_{21}^* & a_{31}^* \\ a_{12}^* & a_{22}^* & a_{32}^* \\ a_{13}^* & a_{23}^* & a_{33}^* \end{bmatrix} \begin{bmatrix} a_{11} & a_{12} & a_{13} \\ a_{21} & a_{22} & a_{23} \\ a_{31} & a_{32} & a_{33} \end{bmatrix} = [I]$$

* See equation 4.1.

Therefore, we get the relation –

$$[U_B^T] = \left[{U_A}^{-1}\right] \qquad 4.2$$

4.1.5 Unit cell and atomic positions

Unit cell is a fundamental repeating unit of a crystal structure. Assuming basis vectors $\boldsymbol{a_1}\ \boldsymbol{a_2}\ \boldsymbol{a_3}$ we can put the atoms in different positions $R_1, R_2, \dots, R_n$. These positions are given by fractional atomic positions x, y, z (equation 4.1) and therefore

$$R = x\boldsymbol{a_1} + y\boldsymbol{a_2} + z\boldsymbol{a_3}\ ;\ 0 \leq x, y, z < 1 \qquad 4.3$$

define the unit cell. Once the unit cell is established, it is possible to locate all atoms within the crystal structure using lattice translations. Meaning, instead of multiplying the basis vector only with x, y, z, we can multiply by $x \pm u,\ y \pm v,\ z \pm w,\ u, v, w \in N$.

4.2 Crystallographic computations

In a Cartesian reference frame calculating distances and angles is an easy task. Using the Pythagorean theorem, we can calculate any distance between two points, and the angle between two vectors could be calculated using the dot product. It gets more complicated when our reference frame is not Cartesian, and we need to use some new tools. The main reason for choosing a non-Cartesian reference frame is due to the periodicity the crystal.

4.2.1 Calculating the dot product within a crystal lattice

For any crystallographic reference frame with basis vectors $\boldsymbol{a_1}, \boldsymbol{a_2}, \boldsymbol{a_3}$ and angles $\alpha_1, \alpha_2, \alpha_3$ the dot product of vectors $\boldsymbol{u}$ and $\boldsymbol{v}$ as shown in Figure 4.5 is given by –

$$u \cdot v = (u_1\ u_2\ u_3)\begin{bmatrix} G_{11} & G_{12} & G_{13} \\ G_{21} & G_{22} & G_{23} \\ G_{31} & G_{32} & G_{33} \end{bmatrix}\begin{pmatrix} v_1 \\ v_2 \\ v_3 \end{pmatrix} \qquad 4.4$$

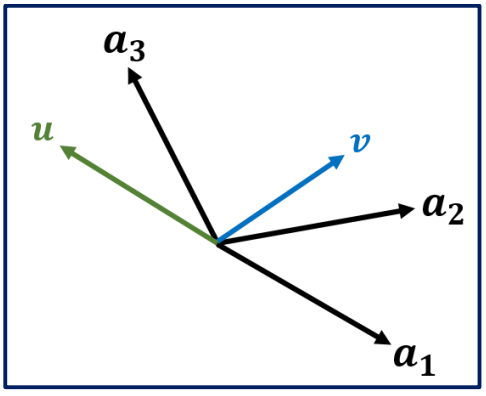

Figure 4.5. Vectors $\boldsymbol{u}, \boldsymbol{v}$ in respect to $\boldsymbol{a_1}, \boldsymbol{a_2}, \boldsymbol{a_3}$ basis vectors

Where G is the matrix of dot product –

$$[G] = \begin{bmatrix} a_1^2 & a_1a_2 & a_1a_3 \\ a_2a_1 & a_2^2 & a_2a_3 \\ a_3a_1 & a_3a_2 & a_3^2 \end{bmatrix} = \begin{bmatrix} a_1^2 & a_1a_2\,cos\alpha_3 & a_1a_3\,cos\alpha_2 \\ a_2a_1\,cos\alpha_3 & a_2^2 & a_2a_3\,cos\alpha_1 \\ a_3a_1\,cos\alpha_2 & a_3a_2\,cos\alpha_1 & a_3^2 \end{bmatrix}$$

In addition, we can define the matrix of reciprocal dot product as –

$$[G^*] = \begin{bmatrix} (a_1^*)^2 & a_1^*a_2^* & a_1^*a_3^* \\ a_2^*a_1^* & (a_2^*)^2 & a_2^*a_3^* \\ a_3^*a_1^* & a_3^*a_2^* & (a_3^*)^2 \end{bmatrix} = \begin{bmatrix} (a_1^*)^2 & a_1^*a_2^*\,cos\alpha_3^* & a_1^*a_3^*\,cos\alpha_2^* \\ a_2^*a_1^*\,cos\alpha_3^* & (a_2^*)^2 & a_2^*a_3^*\,cos\alpha_1^* \\ a_3^*a_1^*\,cos\alpha_2^* & a_3^*a_2^*\,cos\alpha_1^* & (a_3^*)^2 \end{bmatrix}$$

We can get the relation between $[G]$and $[G^*]$ matrices by –

$$[G^*][G] = [U_B^T][U_B][U_A^T][U_A] = [U_B^T][I][U_A] = [I]$$

Therefore, we get that –

$$[G^*] = [G]^{-1} \qquad 4.5$$

4.2.2 Calculating distances within a crystal lattice

The metric tensor contains the same information about the lattice as the lattice parameters, but in a form that is suitable for geometric computations. For any two points q and p we can rewrite the expression for the squared distance between them in a compact notation –

$$D^2 = \sum_{i,j=1}^{N} (q-p)_i G_{ij} (q-p)_j \qquad 4.6$$

where N = 3 in a 3D space, but this definition holds for any finite natural number. In the Einstein notation we will drop the summation sign –

$$D^2 = (q-p)_i G_{ij} (q-p)_j \qquad 4.7$$

In this format $(q-p)_i$ is a row vector, $(q-p)_j$ is a column vector, and G_{ij} are the elements of the metric tensor. For example, taking p as the origin and q = (1,1,1) we get the expression –

$$D^2 = [1\ 1\ 1] \begin{bmatrix} a_1^2 & a_1a_2\,cos\alpha_3 & a_1a_3\,cos\alpha_2 \\ a_2a_1\,cos\alpha_3 & a_2^2 & a_2a_3\,cos\alpha_1 \\ a_3a_1\,cos\alpha_2 & a_3a_2\,cos\alpha_1 & a_3^2 \end{bmatrix} \begin{bmatrix} 1 \\ 1 \\ 1 \end{bmatrix} = \qquad 4.8$$

$$= a_1^2 + a_2^2 + a_3^2 + 2a_1a_2\,cos\alpha_3 + 2a_1a_3\,cos\alpha_2 + 2a_2a_3\,cos\alpha_1$$

For some given lattice parameters, we can then calculate this distance.

4.3 Symmetry

Symmetry is a property of an object, for example unit cell or crystal structure to remain unchanged after applying some kind of movement (*symmetry operation*).

4.3.1 Types of symmetry operations

There are two types of symmetry operations, which correspond to the type of the movement.

1. Point symmetry – During the movement of the crystal at least one point is fixed. E.g. rotation, reflection, inversion and any combination of these operations.
2. Space symmetry – During the movement none of the points is fixed. E.g. translation and any combination of translation and point symmetry operation.

After applying the above symmetry operations, the final position must stay within the unit cell boundaries. In case the final position is outside the unit cell, it has to be reduced back to the following boundaries – $(0 \leq x, y, z < 1)$, by translation.

4.3.2 Matrix description of symmetry operation

Any symmetry operation can be described by a rotation matrix [S], and a displacement vector **d**. In a 3D space [S] is a 3x3 matrix and **d** is a three component column vector –

$$\begin{bmatrix} S_{11} & S_{12} & S_{13} \\ S_{12} & S_{22} & S_{23} \\ S_{31} & S_{32} & S_{33} \end{bmatrix} \begin{pmatrix} d_1 \\ d_2 \\ d_3 \end{pmatrix}$$

Applying a symmetry operation on an arbitrary vector $\mathbf{R_0}$ we get –

$$\boldsymbol{R_1} = [S]\boldsymbol{R_0} + \boldsymbol{d} \qquad 4.9$$

Where {[S], **d**} is the symmetry operation and R_1 is the "new" vector. In a matrix notation we can express this transformation from 4.9 as follows –

$$\begin{pmatrix} x \\ y \\ z \end{pmatrix} \rightarrow \begin{matrix} S_{11}x + S_{12}y + S_{13}z + d_1 \\ S_{21}x + S_{22}y + S_{23}z + d_2 \\ S_{31}x + S_{32}y + S_{33}z + d_3 \end{matrix}$$

The rows of [S] together with the components of **d** are the coordinates of the "new" object, after transformation.

In order to better understand what a symmetry operation is let's look on simple 2D example. Assuming we have a square with l,m,n,o as its vertices located at the positions (3,1), (-1,3), (-3,-1), (1,-3) respectively, and we are given a symmetry operation by the rotation matrix $[S] = \begin{pmatrix} 0 & -1 \\ 1 & 0 \end{pmatrix}$ and a translation vector $\boldsymbol{d} = \begin{pmatrix} 1 \\ 2 \end{pmatrix}$. In Figure 4.6 we can see

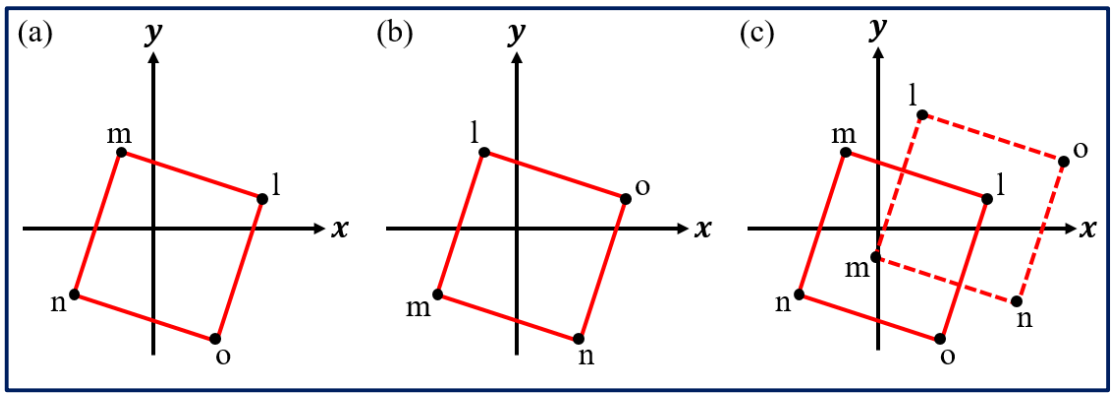

Figure 4.6 Symmetry operation applied on a square in a 2D space

what happens to the square after multiplying with [S] matrix, and after adding the translation vector **d** (Figure 4.6b and 3.6c). It's easy to check what happens to vertex l (3,1) after multiplying with [S] matrix – $\begin{pmatrix} 0 & -1 \\ 1 & 0 \end{pmatrix}\begin{pmatrix} 3 \\ 1 \end{pmatrix} = \begin{pmatrix} -1 \\ 3 \end{pmatrix}$. We get in general that any point (x,y) is transformed to – $\begin{pmatrix} 0 & -1 \\ 1 & 0 \end{pmatrix}\begin{pmatrix} x \\ y \end{pmatrix} = \begin{pmatrix} -y \\ x \end{pmatrix}$. Therefore, the square is rotated 90^0 degrees counterclockwise on each operation. Adding the vector **d** simply translates the square one unit to the right and two units upward.

4.3.3 Combination of symmetry operations

In case we want to combine two symmetry operations $\{[S^1], \boldsymbol{d^1}\}$ and $\{[S^2], \boldsymbol{d^2}\}$, we will get the following relations –

$$\boldsymbol{R_2} = [S^2]\boldsymbol{R_1} + \boldsymbol{d^2} = [S^2][S^1]\boldsymbol{R_0} + [S^2]\,\boldsymbol{d^1} + \boldsymbol{d^2} \qquad 4.10$$

Where $\mathbf{R_1}$ is taken from equation 4.9.

The rotation matrix of the combination of the symmetry operations S^{comb} equals to the multiplication of matrices $[S^2][S^1]$, and the displacement vector $\boldsymbol{d^{comb}}$ is $[S^2]\,\boldsymbol{d^1} + \boldsymbol{d^2}$. Since matrix multiplication is not commutative it is clear that the combination of symmetry

operations is not commutative as well. Meaning that the order we apply the symmetry operations may affect the final result.

4.3.4 Symmetry group

Symmetry group is a group of movements (operations) describing symmetry operations. There are some requirements for a mathematical group such as – closure, existence of identity element, associativity and invertibility.

Point symmetry group – Since the symmetry of the crystal is a combination of the symmetry of the lattice and the unit cell, the symmetry of the crystal can be equal or lower than the symmetry of the lattice. If we list all possible combinations of point symmetries, we get 32 crystallographic point groups. If the point group of the crystal is equal to the point group of the lattice, it is called holohedry. In 3D space there are 7 holohedries (7 crystal systems). In order to get all point symmetry groups one needs to take out symmetry elements from the crystal system, one at a time. In this way we get the symmetry groups for the different crystals.

Space group – A crystallographic space group is the symmetry group of a crystal structure. Therefore, it contains all the symmetry operations of this crystal. There are 230 space groups in 3D space, also called Fedorov groups, after the Russian mathematician, crystallographer and mineralogist Evgraf Stepanovich Fedorov. The different elements of space groups are in fact transformation between crystallographic coordinate systems which are symmetry equivalent. These transformations can be described by symmetry operations, meaning rotation matrix [S], and displacement vector d (sub-section 3.3.2).

There are two requirements which must be filled to create a space group –

1. Closure – any combination of symmetry element within the group must stay in the group. For a compact description of a space group we may want to introduce the minimum symmetry elements which build the entire group. These elements are called generators.
2. Identity- any space group must include the identity element. In this case the identity element includes the identity matrix and a translation vector –

$$S = \begin{pmatrix} 1 & 0 & 0 \\ 0 & 1 & 0 \\ 0 & 0 & 1 \end{pmatrix} \quad d = \begin{pmatrix} u \\ v \\ w \end{pmatrix}$$

Where u, v, w are integers describing the lattice translation.

4.3.5 Wyckoff positions

A position x, y, z (fractional coordinates) is called general position if the number of points in the unit cell which are symmetry equivalent to x, y, z is equal to the order of the group, otherwise, it's called a special position. The number of symmetry equivalent points is called multiplicity. Wyckoff position contains the information about equivalent positions in the unit cell, labelled consecutively – a, b, c ...(Wyckoff letter), starting with a for the highest symmetry. It also contains a number to the left of the letter, indicating the multiplicity of this position.

4.4 Lattice planes

Lattice planes (crystallographic planes) are any set of parallel and equally spaced planes, intersecting the center of the atoms in a crystal structure, where no atoms are situated in between them. For 2D lattices the planes are considered as lattice rows, and for 3D lattices those are lattice planes. In this chapter we will mostly dill with lattice rows (2D lattices), which will be called lattice planes (degenerated planes).

4.4.1 The equation of a lattice plane

The most fundamental equation of a lattice plane for the 2D case is given by –

$$h_1 x + h_2 y = N \qquad 4.11$$

Where h and k are mutually prime numbers, describing the directionality of the plane, and N is the number of the plane. Plane number 0 is the one that crosses the origin, and N is just a serial number counting the planes, as shown in Figure 4.7. In this figure the origin is fixed at point O with $\boldsymbol{a_1 a_2}$ as the basis vectors. The plane introduced in the figure by red lines are parallel to each other, and the are no lattice points in between two adjacent planes. They are numbered in ascending order starting from zero at the origin (point O).

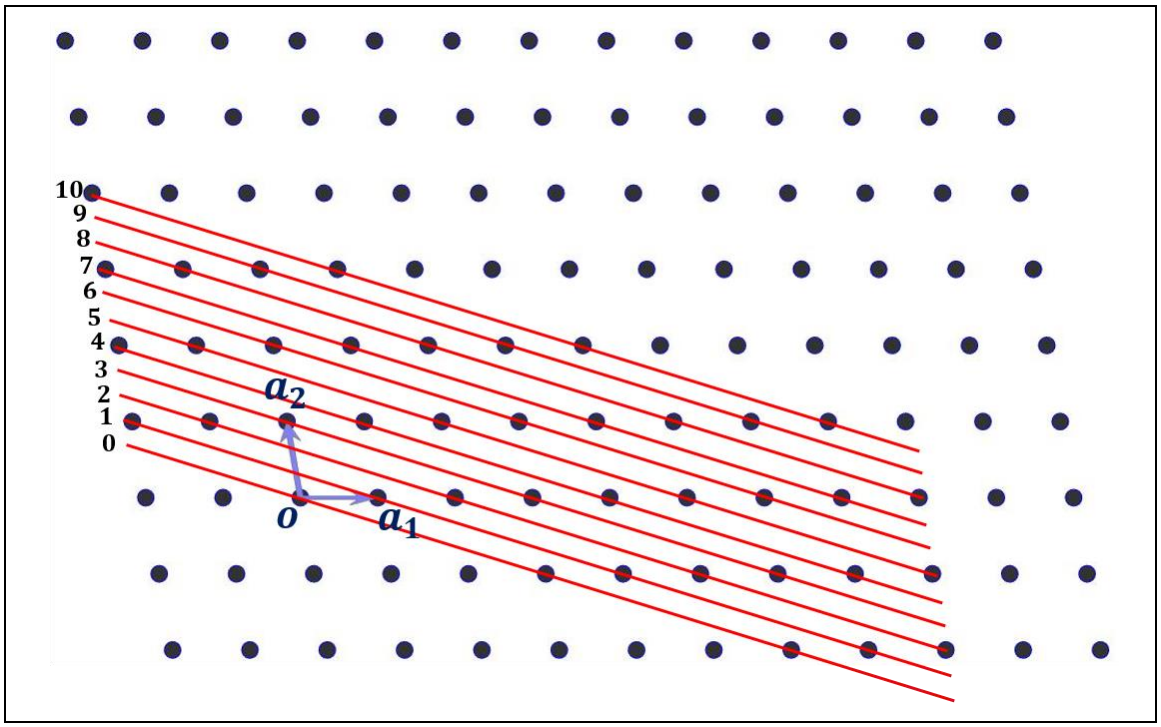

Figure 4.7. 2D lattice with basis vectors $a_1 a_2$ and a set of lattice numbered in respect to the origin O

4.4.2 Interplanar distance and Miller indices

Assuming we have to vectors A and B, which are given by –

$$\boldsymbol{A} = u_1\boldsymbol{a_1} + u_2\boldsymbol{a_2} \; ; \; \boldsymbol{B} = h_1\boldsymbol{a_1^*} + h_2\boldsymbol{a_2^*}$$

Where $\boldsymbol{a_1 a_2}$ are basis vectors, $\boldsymbol{a_1^* a_2^*}$ are reciprocal basis vectors, and u_1, u_2, h_1, h_2 are integers. Applying the dot product between A and B we get

$$\boldsymbol{A} \cdot \boldsymbol{B} = u_1 h_1 + u_2 h_2$$

From this equation which derives a new form of equation 4.11 as

$$\boldsymbol{R} \cdot \boldsymbol{B} = N \qquad 4.12$$

Where **R** is given by $A_1 + tA_2$, t is an arbitrary number, A_1, A_2 are vector on plane number one and zero respectively, as shown in Figure 4.8. In this way **R** describes the equation of plane number 1. From equation 4.12 we get two important conclusions: (1) For plane number zero we get $\boldsymbol{R} \cdot \boldsymbol{B} = 0$. Meaning, the reciprocal lattice vector **B** is perpendicular to the plane. (2) For plane number one we get $\boldsymbol{R} \cdot \boldsymbol{B} = 1$. Meaning that the *interplanar distance* (the distance between two adjacent parallel planes) is

$$d = B^{-1} \qquad 4.13$$

Where B is the length of the reciprocal lattice vector.

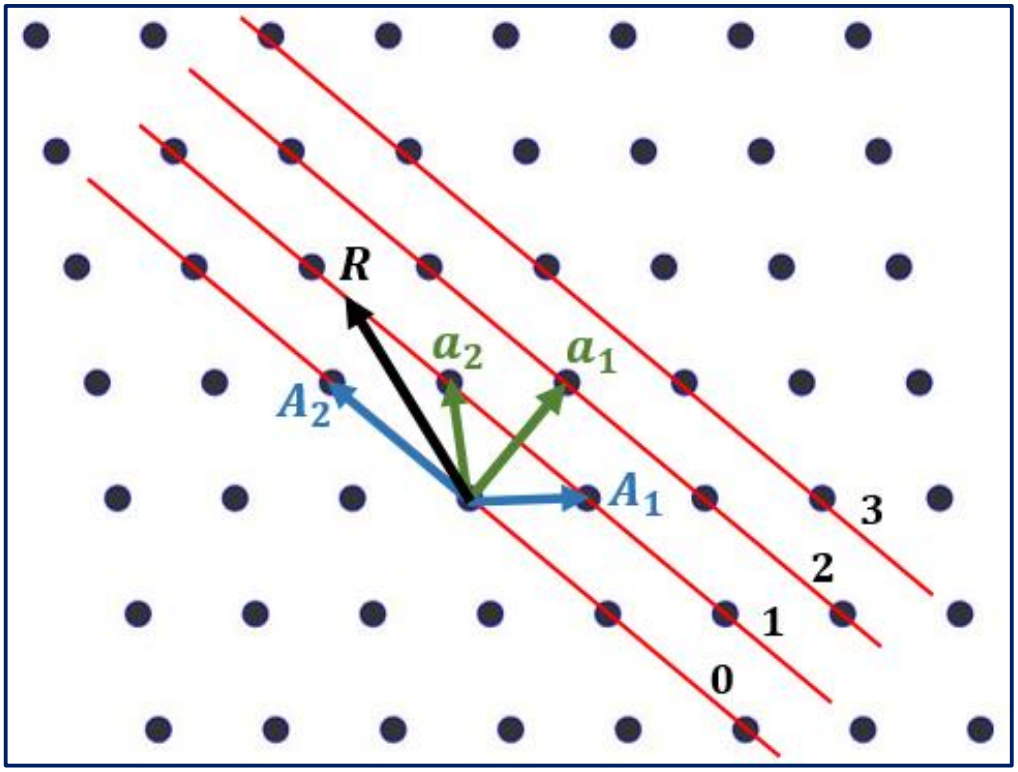

Figure 4.8. 2D lattice with two sets of basis vectors $a_1 a_2$ and $A_1 A_2$. R is a vector laying in plane 1; R is given by $\boldsymbol{A_1 + tA_2}$. For $\boldsymbol{t} \in (-\infty, \infty)$, the vector **R** can describe any point on plane number 1.

Each set of rows can be described by integer numbers (h_1, h_2) known as *Miller indices*. According to the definition of those numbers they are mutually prime integers. The reciprocal lattice vector $\boldsymbol{B} = h_1\boldsymbol{a_1^*} + h_2\boldsymbol{a_2^*}$ is perpendicular to the set of $(h_1 h_2)$ planes.

For 3D lattices the definitions and equations can be easily extended. The equation of planes can be written as

$$h_1 x + h_2 y + h_3 z = N \qquad 4.14$$

Each set of lattice planes is described by three mutually prime numbers $(h_1 h_2 h_3)$, the Miller indices of the plane. Accordingly, the reciprocal lattice vector is

$$\boldsymbol{B} = h_1\boldsymbol{a_1^*} + h_2\boldsymbol{a_2^*} + h_3\boldsymbol{a_3^*}$$

Where $(\boldsymbol{a_1^* a_2^* a_3^*})$ are the reciprocal basis vectors. Equation 4.13 still holds for the interplanar distance. From this equation we see that B is inversely proportional to d,

meaning that the higher the Miller indices of a plane, the smaller the interplanar distance between them.

5 Electron density

The time average electron density $\langle \rho(\boldsymbol{r}) \rangle$ is calculated by the weighted average of the electron density along the nuclear vibration path. The weights are determined by the nuclear probability distribution $NPD(u_1, u_2, \dots, u_N)$, where $u_1, u_2, \dots, u_N$ being the displacement coordinates. We get that if $\rho(\boldsymbol{r}, u_1, u_2, \dots, u_N)$ is the electron density at position r corresponding to the nuclear geometry which determined by $u_1, u_2, \dots, u_N$, the time averaged electron density would be[28]

$$\langle \rho(\boldsymbol{r}) \rangle = \int \rho(\boldsymbol{r}, u_1, u_2, \dots, u_N) NPD(u_1, u_2, \dots, u_N) du_1 du_2 \dots du_N \quad 5.1$$

The density for a rigid group where the electrons can be assigned to specific nuclei (for example a crystal) will follow the equation –

$$\langle \rho_{RG}(\boldsymbol{r}) \rangle = \int \rho_S(\boldsymbol{r} - \boldsymbol{u}) NPD(\boldsymbol{u}) d\boldsymbol{u} = \rho_S(\boldsymbol{r} - \boldsymbol{u}) * NPD(\boldsymbol{u}) \quad 5.2$$

Where ρ_{RG} is rigid group density, and ρ_S is the static density. In total we get –

$$\langle \rho_{atom}(\boldsymbol{r}) \rangle = \rho_{atom,static}(\boldsymbol{r}) * NPD(\boldsymbol{u}) \quad 5.3$$

Which is known as the convolution approximation. In case $\rho_{atom,static}(\boldsymbol{r})$ is a delta function in respect to the nucleus, we get the relation –

$$\langle \rho_{atom}(\boldsymbol{r}) \rangle = \delta(\boldsymbol{r}) * NPD(\boldsymbol{u}) = NPD(\boldsymbol{u}) \quad 5.4$$

5.1 Probability density function

The Probability Density Function (PDF) is used to specify the probability of a random variable falling within a particular range of values. In our case, we will use this function to calculate the NPD, meaning the probability of finding an atom within a certain volume in space. In order to do so, one must calculate the integral of this function, within the desired volume. The integral over the entire space is equal to 1. For anisotropic potential the PDF function in matrix notation is given by[28]

$$PDF = \frac{|\sigma^{-1}|^{1/2}}{(2\pi)^{3/2}} exp\left(-\frac{1}{2}\boldsymbol{u}^T\sigma^{-1}\boldsymbol{u}\right) \quad 5.5$$

Where $\boldsymbol{u} = \begin{bmatrix} x - x_0 \\ y - y_0 \\ z - z_0 \end{bmatrix}$, the position of the atom center in respect to (x_0, y_0, z_0), T is the transpose operation, and σ is a standard information obtained by x-ray diffraction experiment and will be explained later.

5.2 Atomic displacement parameters

Atomic Displacement Parameters (ADPs) also called thermal displacements indicate the magnitude and direction of thermal vibrations of atoms in crystals. We are often interested in the rms thermal vibrations in angstrom units, which correspond to the contravariant $[U]$ components along covariant axes of unit length. The rms displacements are obtained by[28]

$$[\beta] = 2\pi^2[U] * \left[\begin{pmatrix} a_1^* \\ a_2^* \\ a_3^* \end{pmatrix} (a_1^* \quad a_2^* \quad a_3^*)\right] = \quad 5.6$$

$$= 2\pi^2[U] * \begin{bmatrix} (a_1^*)^2 & a_1^*a_2^* & a_1^*a_3^* \\ a_2^*a_1^* & (a_2^*)^2 & a_2^*a_3^* \\ a_3^*a_1^* & a_3^*a_2^* & (a_3^*)^2 \end{bmatrix}$$

The symbol $*$ refers to an element-wise multiplication and a_1^*, a_2^*, a_3^* are the reciprocal lattice parameters. Finally we get $[\sigma]$ which contains the ADPs –

$$[\sigma] = [UA][\beta][UA]^T \quad 5.7$$

Where $[UA]$ is the orientation matrix of the crystal structure, and T is the transposed operation.

5.3 Average atomic density

For a given atomic density $D(x, y, z)$, the average atomic density (AAD) for a (001) plane is given by –

$$M(z) = \langle D(x, y, z)\rangle = \frac{\iint D(x, y, z)dA}{\iint dA} \quad 5.8$$

Where $M(z)$ is the AAD, and it depends only on the z coordinate, and dA is a surface element parallel to (001) plane.

Figure 5.1 illustrates the concept of function $M(z)$ where the atoms are geometrically visualized as spheres for the α-SiO_2 crystal structure. The area of the atoms intersecting (001) planes is calculated for each of the sections, and divided by the area of the plane. This calculation is limited to one unit cell, and we will discuss this topic later in this work.

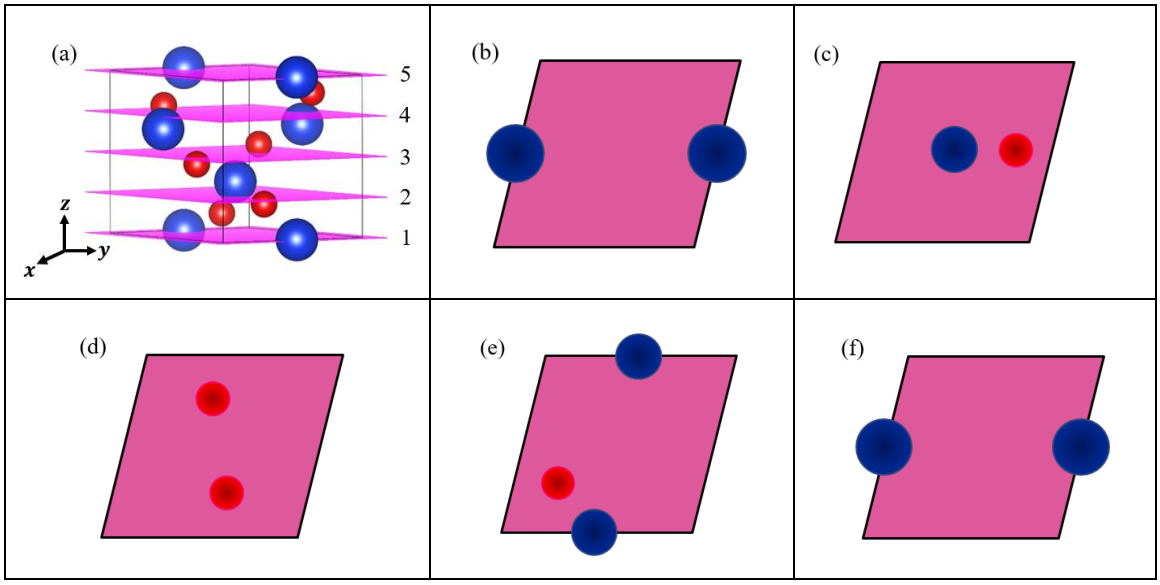

Figure 5.1. Different section of (001) plane in α-SiO_2 crystal structure;
(a) All different sections a 3D figure. (b)-(f) Describe top view of 1-5 sections

6 Building the Model

6.1 Model assumptions

1. Crystal structure is periodic.
2. Cleavage analysis can be restricted to the unit cell level.
3. Any lattice plane can become (001) choosing the "right" unit cell.
4. Cleavage is related to structure.

The first The first assumption relies on the periodicity of a crystal structure. It means that the crystal can be built using the information about the symmetry-independent atoms (their Wyckoff positions), the symmetry operations of the crystal structure and the ADPs of the atoms.

The second assumption derives from the periodicity of the crystal structure. We will calculate the average atomic density on a single unit cell, for different planes and along different sections. It is quite obvious that these calculations are valid for any unit cell in the crystal.

The third assumption requires some explanation. Assuming we have a 2D lattice with basis vectors $(\boldsymbol{a_1 a_2})$, as shown in Figure 6.1. Sub-figure (a) describes (10) planes in respect to a standard unit cell with $(\boldsymbol{a_1 a_2})$ as its basis vectors. In 6.1(b) we can see how the former plane becomes (01) in respect to a different choice of the unit cell, this time with $(\boldsymbol{A_1 A_2})$ as the basis vectors. The same process was performed in 6.1(c) and 6.1(d), where the original plane was $(\bar{2}3)$, and it ended up as (01).

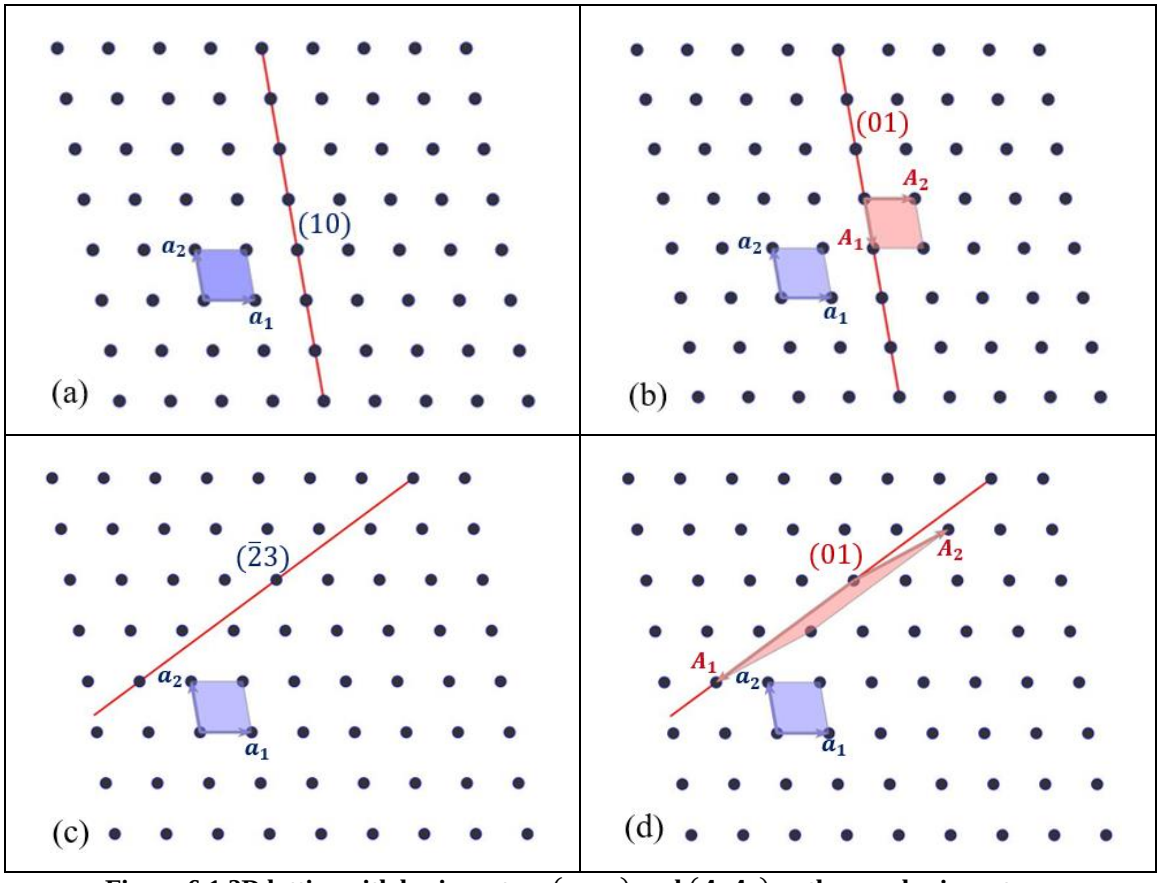

Figure 6.1 2D lattice with basis vectors $(\boldsymbol{a_1 a_2})$ and $(\boldsymbol{A_1 A_2})$ as the new basis vectors;

(a) (10) plane in respect to $(\boldsymbol{a_1 a_2})$, (b) (01) plane in respect to $(\boldsymbol{A_1 A_2})$, (c) $(\bar{2}3)$ plane in respect to $(\boldsymbol{a_1 a_2})$, (d) (01) plane in respect to $(\boldsymbol{A_1 A_2})$

We come up with the conclusion that indices of every plane can become (01) plane by the appropriate transformation of the unit cell. The main principle for that choice is that $\mathbf{A_1}$

(the new basis vector) will be parallel to the plane . The very same concept applies for 3D crystals, where we want to convert any lattice plane to (001). Again, by choosing an appropriate transformation of a unit cell the basis vectors $(\mathbf{A_1 A_2})$ create a plane parallel to the original plane. In this way we assure that the original plane in respect to the new unit cell will be (001).

Regarding the forth assumption, we simply say that once a crystal structure is given, the average atomic density can be calculated for any plane and any section of the plane. The lower the average atomic density is, the higher the tendency of this plane to cleave would be. Visually, for sections of planes with a low average atomic density values, it looks as if there are gaps in between adjacent parallel planes, as shown in Figure 3.4.

6.2 Cleaving ability

One of the most important parameters in our model as described earlier in this work is the average atomic density. In order to evaluate how likely is a certain plane to become a cleavage plane we came up with a new definition – cleaving ability (CA). We defined CA as the inverse of the average atomic density. For the case of (001) plane it's simply given by –

$$CA(z) = \frac{1}{\langle D(x,y,z) \rangle} = \frac{1}{M(z)} \qquad 6.1$$

Where M(z) is the average atomic density, and it depends only on the z coordinate.

6.3 Graphene – 2D example

6.3.1 Graphene structure

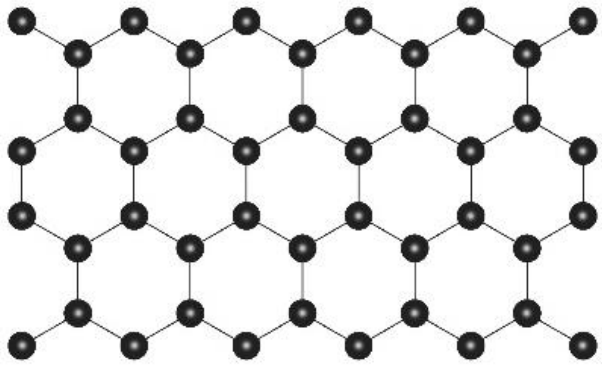

Crystal system: Hexagonal

Planar space group: $p6mm$ (17)

Point group: $3m$

Lattice parameter: a = 2.46 Å

Unit cell: C [1/3,2/3] 2b

Atomic displacement parameters: [0.0031,0.0031,0.0016]

Table 6-1. Crystal structure and crystallographic information of graphene;
The information was adopted from graphite crystal strucure[29]

6.3.2 Graphene cleavage investigation

Using the crystallographic information described in Table 6-1, a standard unit cell was built for the graphene structure. We started by investigating the (01) plane, where in this process the average atomic density was calculated along the $\mathbf{a_1}$ direction for different y section.

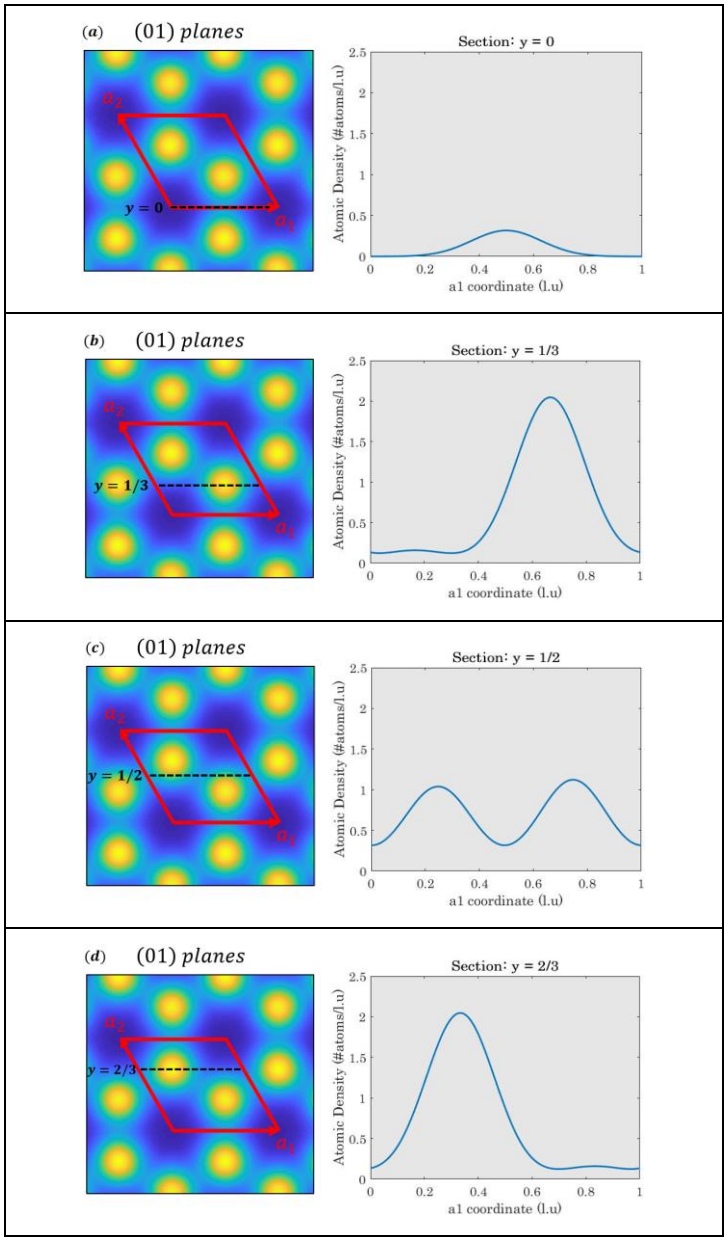

Figure 6.2 Graphene different sections and atomic density calculations along a_1 on (01) planes;
In each of the sections the average atomic density is plotted for different sections on a_2 coordinate

This process was repeated for different crystallographic planes. As shown in Figure 6.1, for every lattice plane other than (01), the unit cell was transformed in such a way that it became (01) plane. In this manner, all we had to do was first transforming the unit cell, and second, repeating the same algorithm. Figure 6.3 describes a complete scanning of all possible planes, calculating the average atomic density M(z) and the CA. Figure 6.3b shows all the cleavage planes found in the process. There are only (01) and (11) planes with relatively high CA values, and its family members. Every point in between the peaks is denoted by a different lattice plane, where the CA values of all the planes are pretty similar (besides (01) and (11) planes). The distance from the center represents the CA of a certain lattice plane, and for the (01) plane the CA value is ~2.2 times bigger than for the (11) plane. Figure 6.3a shows these planes on a standard unit cell, where we also notice the big gaps which enables the cleavage.

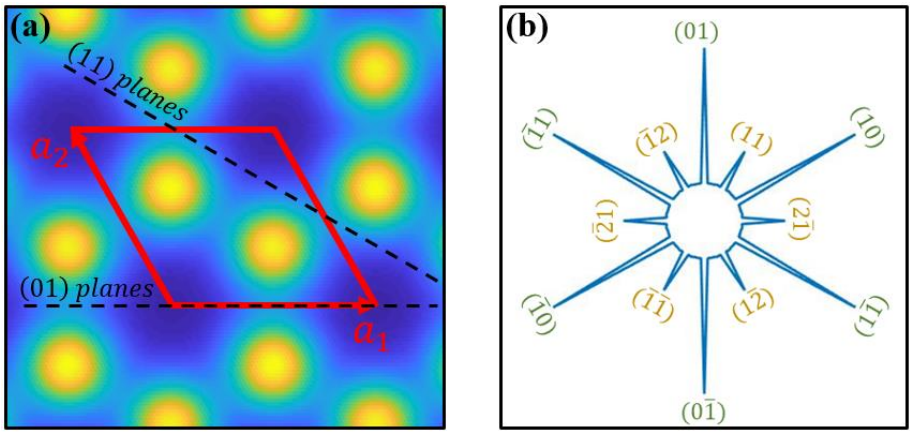

Figure 6.3 Describe the CA values of all possible lattice planes in graphene structure;
(a) presents (01) and (11) planes. (b) complete scan of CA values of different planes.

7 Results

In this chapter we will describe the process of applying the model on the structures of – Silicon, Lithium Niobate and α-Quartz. We will describe this process in details in the next sub-section, but the general flow will be as follows –

1. Using a CIF file of each structure to build and fill the unit cell with atoms.
2. Creating a list of lattice planes.
3. Each plane was represented by a different unit cell, in such a way that it's indices were (001).

4. The unit cell was divided into N sections (usually N = 100 was chosen) along the a_3 coordinate, and for each section CA was calculated. The minimum CA of each plane was marked and saved.
5. The list of minimum CA's was plotted vs miller indices of the planes using stereographic projection.

7.1 Silicon

Silicon crystallizes with the diamond structural type. Each atom on the silicon structure has four nearest neighbors, creating a tetrahedral coordination as shown in the figure below. The mechanical and physical properties of silicon are well known in literature, after a comprehensive research in the last decades[30–33]. Silicon has two cleavage planes (111) and (110), with cleavage energies of 2.88 and 3.46 $\mathrm{J/m^2}$ respectively[3]. Table 7-1 summarizes some relevant information of the silicon structure which will later be used to apply our model, following the 5 steps described above.

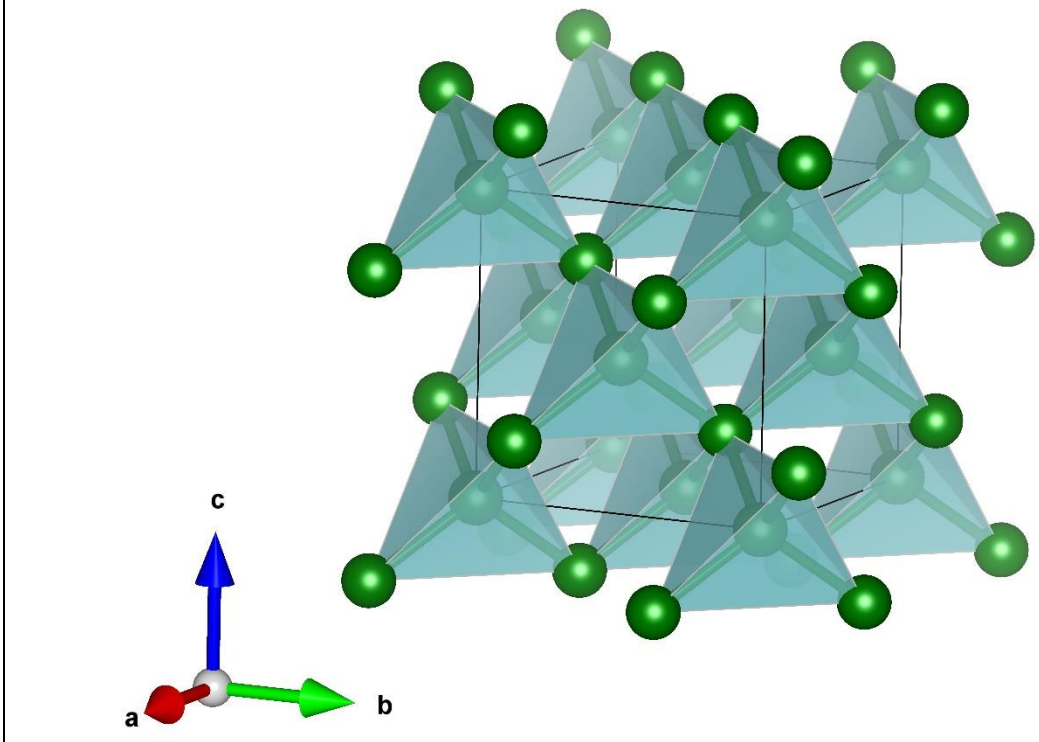

Crystal system: Cubic Lattice parameters:	Atomic displacement parameters: U_{11} U_{22} U_{33} U_{23} U_{13} U_{12}

$a_1 = a_2 = a_3 = 5.43\text{Å}$ $\alpha = \beta = \gamma = 90^0$ Space group: $Fd\bar{3}m$ (227) Point group: $m\bar{3}m$ Unit cell: Si [0, 0, 0] 8a	[0.0072, 0.0072, 0.0072, 0, 0, 0] Position of atoms (fractional coordinates): [0,0,0], [0.25,0.25,0.25], [0,0.5,0.5], [0.25,0.75,0.75], [0.5,0.5,0], [0.5,0,0.5] [0.75,0.25,0.75], [0.75,0.25,0.75]

Table 7-1. Crystal structure and crystallographic information of Si;
At the top – VESTA image of silicon stucture[20]. At the bottom – Crystal system, lattice parameters, space group, point group, unit cell, ADPs and position of atoms are described[34]

7.1.1 Building the unit cell

Using the information stored in Table 7-1 the positions of all the atoms in the unit cell were calculated. The lattice parameters helped us to calculate the orientation matrix $[U_A]$ (sub-section 3.1.4). The information of the atomic number, $[U]$ values and symmetry independent atoms (in the case of Si only [0,0,0]) was gathered. $[U]$ values were used to calculate $[\sigma]$ (the ADPs) using equations 5.6-5.7.

In order to calculate the atomic density, we had to make a few steps. We ascribed for each point in space a value, referring to the probability to find an atom within this point. Of course that in the continuous case, the probability to find an atom within a specific point is zero, but our unit cell was divided into a finite number of points (the discrete case). 3D grid was defined for x, y, z in the range of 0 to 1, divided to N equally spaced points for each coordinate. This process stands for establishing N^3 points equally spaced within a cube with sides equal 1. The crystallographic coordinates of all the grid points in the unit cell were transformed into Cartesian coordinates by multiplying with $[U_A]$. The next step was to find all lattice points within a sphere which contains the unit cell and a couple of spare angstroms. In order to do so, first we applied all symmetry operations on the position of the Si atom. The symmetry operations were also applied on $[\sigma]$, and its ADPs. Then we had to convert the unique positions into Cartesian coordinates multiplying by $[U_A]$. The final step was to apply the PDF function on each of the lattice points found inside the sphere. By saying "applying" the PDF function on a specific atom we mean that the input parameters were the position of the atom and its ADPs. These inputs were inserted to equation 5.5, so the probability of finding the atom in each small interval in space was calculated. This probability was multiplied by the atomic number of each atom and

summed up. In this way we filled our predefined volume which is the unit cell, with grid containing the information of finding an atom on each point on this grid.

7.1.2 Creating list of lattice planes

At this step the goal was to create a list of planes which will later be used to calculate the CA for each of them. The first list we created was a combination of three integers ranging from $-\left\lfloor\frac{a_i}{d_{min}}\right\rfloor$ to $+\left\lceil\frac{a_i}{d_{min}}\right\rceil$, a_i being the lattice parameters, and i = 1,2,3. In this way we got the boundaries of the indices which correspond to the length of the reciprocal lattice vector. It just had to obey the most basic rule of indexing planes, three mutually prime integers. Another condition we set was that the interplanar distance will not be smaller than d_{min}. For most of our purposes d_{min} = 1Å was a good choice, and in this way we eliminated planes with high indices that are not contributing for our calculations. In this case we chose d_{min} 1Å, since no additional planes with high CA values were discovered below that value. Since there were no symmetry restrictions while creating the list, it included a lot of symmetry equivalent planes. Each group of symmetry equivalent planes is considered as a family of planes. For each family an index was given, and each of the members in the family got this index. In this way, we could easily identify to which family each plane belongs and the computation time could be reduced significantly.

The second list was a reduced version of the first list. Instead of taking all the planes, only symmetry independent planes were taken. That was done for the same reason we indexed the first list, to help us when making preliminary estimations with relatively fast calculations.

7.1.3 Transforming the unit cell

At this stage we have a big group of lattice planes (thousands of planes), and a smaller group with doesn't contain the symmetry equivalent planes, which is still quite big (hundreds of planes). The following steps will include some complicated calculations, so in order to work in a more repetitive and compact manner, we came up with a new idea. For each of the lattice planes the unit cell will be transformed in such a way that in respect to its new basis vector (after transformation), this plane becomes (001) plane (see section 6.1). The concept behind this idea is that all the calculations we have after the transformation will have the same form.

7.1.4 Calculating cleaving abilities

In this step we are about to calculate the CA for each of the planes from the reduced list we created on section 7.1.2. After transforming each of the planes to (001) we had to make an iterative process which calculates CA values. On the first step (section 0) we built the fundamental unit cell, and calculated the accumulated PDF on each point in the unit cell grid. Let's call this property SumPDF. Therefore, what we had to do here was to interpolate SumPDF values for the transformed unit cell, corresponding to its lattice plane. Then, the unit cell was divided to N sections along the $\boldsymbol{a_3}$ coordinate, where N value was usually 100. Since the information about SumPDF was now available (after the interpolation), we could calculate SumPDF for each of the sections and the minimum value was found. Therefore, we defined that the CA of a lattice plane is the inverse of the minimum SumPDF value. In simple words, the least dense section of the unit cell will have the highest CA value, and it implies how likely is the crystal to cleave along this plane. If we stick to our hypothesis (section 6.1), as the average atomic density goes down, the tendency to cleave increases. In fact, we calculated the CA of the reduced list, but it was easily extended to the full list of planes which were indexed according to its equivalent planes.

7.1.5 Plotting CA values vs Miller indices

The final step was to create a plot which encapsulates all the information about CA values of the different lattice planes, as shown in Figure 7.1. The method we chose to present this plot was stereographic projection. In this plot each point represents a reciprocal direction which is normal to a lattice plane. Bold and colored points represents reciprocal directions normal to lattice planes with high CA values. The minimum interplanar distance was set as d_{min} = 1Å. We can see on this plot two families of planes (111) in pale blue, and (110) in gray, with CA values of $55.77\ Å^3/e$ and $8.99\ Å^3/e$ respectively. The size of the different points reflects the differences in CA values (not in accurate scale). Table 7-2 summarizes the cleavage energies and CA values.

Lattice plane	{111}	{110}
CA $[Å^3/e]$	55.77	8.99
$\Gamma_0[J/m^2]$	2.88	3.46

Table 7-2. Cleavage energies and CA values of Si crystal structure[3]

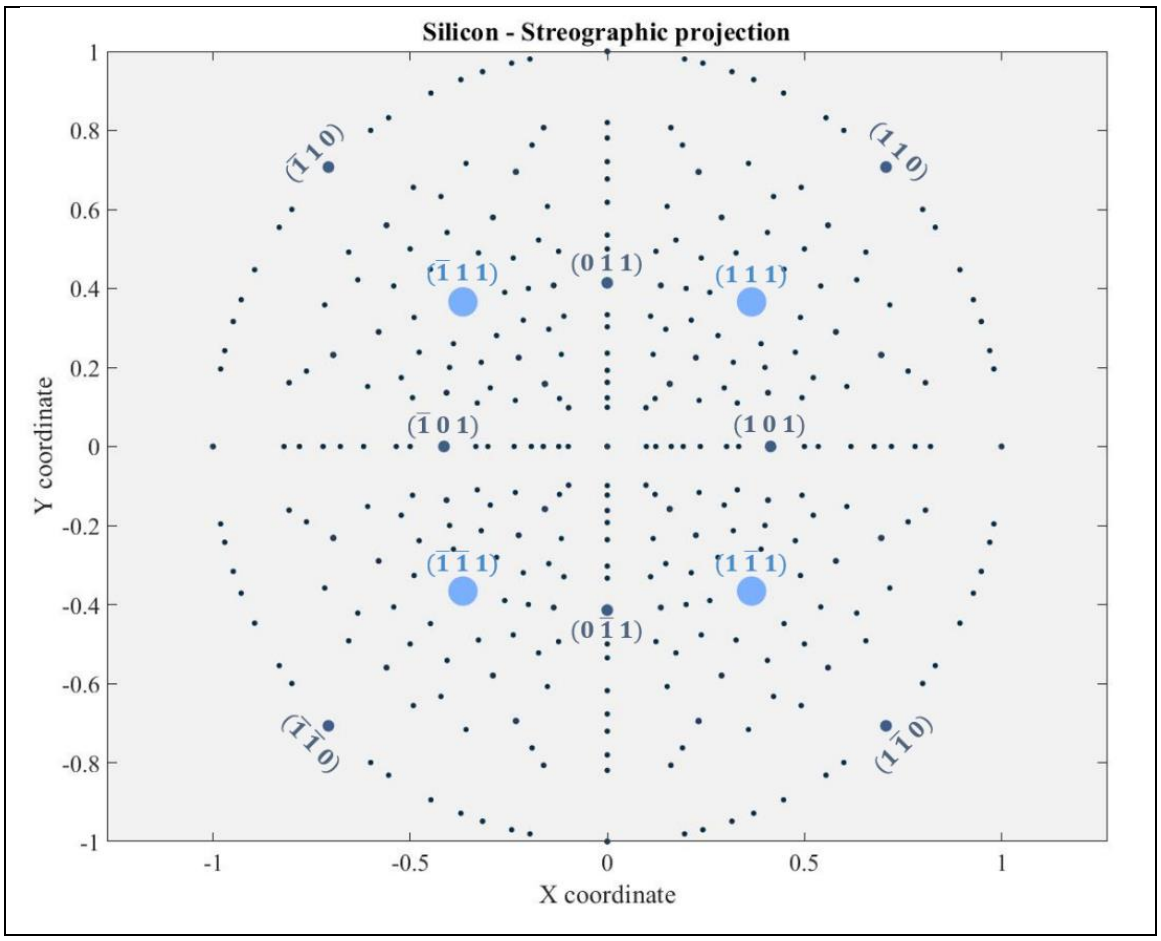

Figure 7.1. Streographic projection of reciprocal directions of silicon reciprocal lattice;
Each point represents a reciprocal direction which is normal to a silicon lattice plane

In Figure 7.2 our algorithm is visualized for (110) and (111) planes. Figure 7.2a describes an internal unit cell scan along the z* direction (parallel to [100] direction) for the (110) plan. The maximum CA value is obtained at z* = 0.25 and z* = 0.75, so the CA for this plane is 8.99 $[Å^3/e]$. These sections are plotted in Figure 7.2b, and it's possible to see that they have very low average atomic density. Figure 7.2c describes the same process for the (111) plane. In this case the maximum value is obtained at z* = 0.38, and the CA for this plane is 55.77 $[Å^3/e]$.

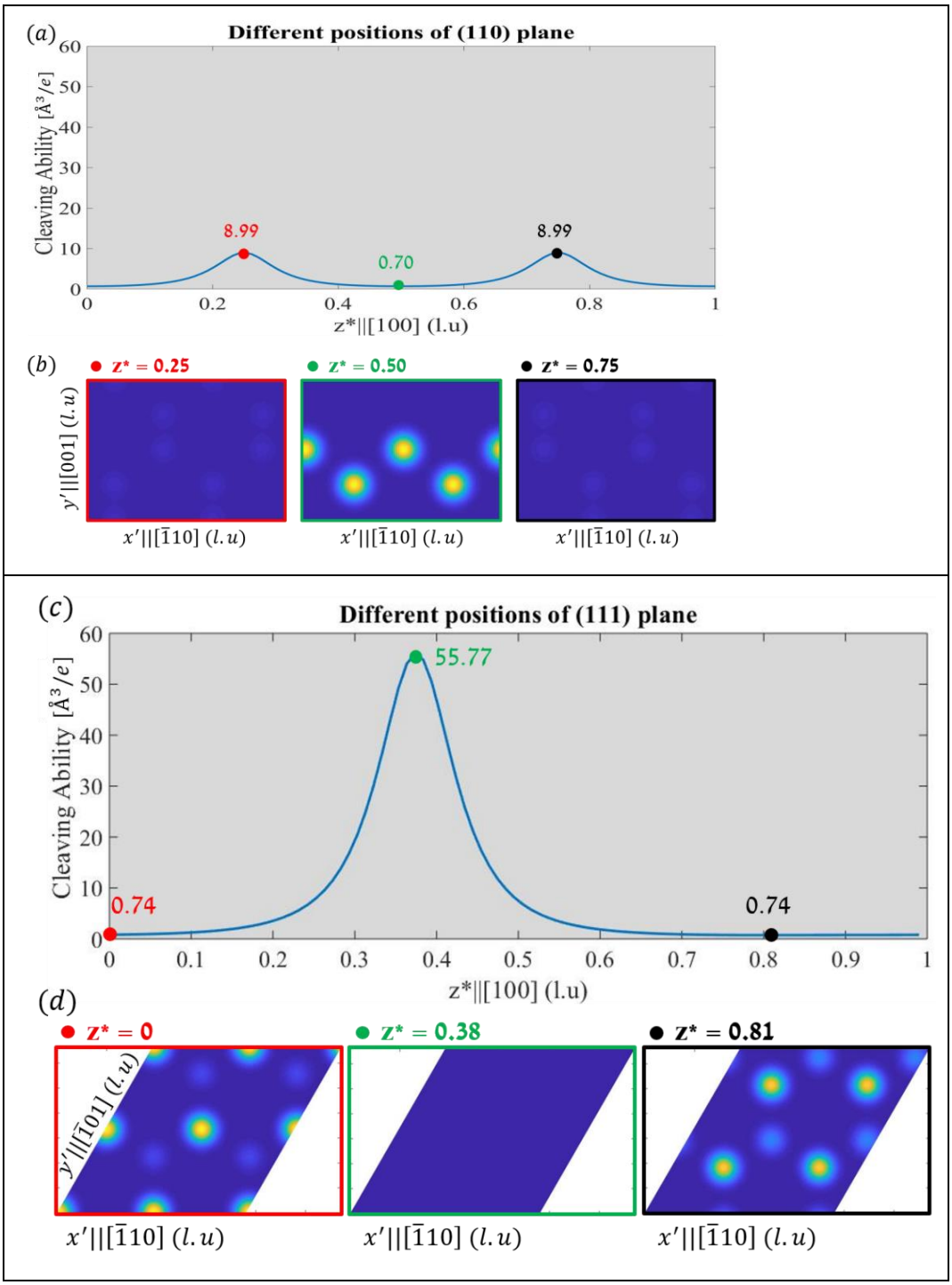
(a)
Different positions of (110) plane
Cleaving Ability [Å³/e]
8.99
0.70
8.99
z*||[100] (l.u)
(b)
z* = 0.25
z* = 0.50
z* = 0.75
y'||[001] (l.u)
x'||[1̄10] (l.u)
x'||[1̄10] (l.u)
x'||[1̄10] (l.u)
(c)
Different positions of (111) plane
Cleaving Ability [Å³/e]
55.77
0.74
0.74
z*||[100] (l.u)
(d)
z* = 0
z* = 0.38
z* = 0.81
y'||[1̄01] (l.u)
x'||[1̄10] (l.u)
x'||[1̄10] (l.u)
x'||[1̄10] (l.u)

Figure 7.2. CA values and different sections of (110) and (111) planes of Si crystal structure;
(a) Cleaving ability of plane (110) vs z* coordinate (||[100]). (b) Images of different sections of (110) plane along z*. (c) Cleaving ability of plane (111) vs z* coordinate (||[100]). (d) Images of different sections of (111) plane along z*.

7.2 Quartz

The second crystal structure analyzed was α-Quartz (α-SiO_2). Quartz structure is a continuous framework of silicon-oxygen tetrahedral, where each of the oxygen atoms is shared between two tetrahedral. Quartz attracts a lot of interest during the last years and an ongoing research[35–38], mainly due to its unique mechanical and optical properties and the potential applications[39–43]. Quartz has known cleavage planes – (110), (011), (111), (010) and (001) with cleavage energies of 8.88, 9.30, 10.90, 11.52 and 12.28 J/m^2 respectively[44]. The relevant information on quartz is introduced in Table 7-3.

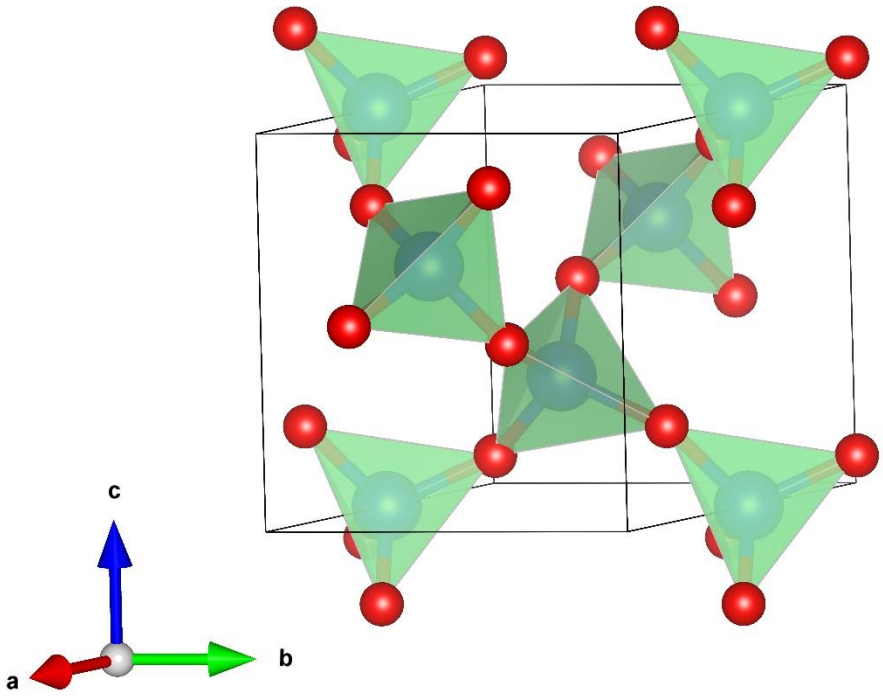

Crystal system: Trigonal Lattice parameters (hexagonal setting): $a_1 = a_2 = 4.91Å \ a_3 = 5.41Å$ $\alpha = \beta = 90^0 \ \gamma = 120^0$ Space group: $P3_221$ (154)	Atomic displacement parameters: Si [0.0086, 0.0072, 0.0073, -0.00002, -0.00001, 0.0036] O [0.0175, 0.0132, 0.0123, -0.0041, -0.0029, 0.0097]

Point group: $3m$	Position of atoms (fractional coordinates):
Unit cell:	O: [0.41,0.27,0.12], [0.27,0.41,0.55], [0.85,0.59,0.45]
Si [0.47, 0, 0] 3a	[0.14,0.73,0.88], [0.59,0.85,0.21], [0.73,0.15,0.79]
O [0.41, 0.27, 0.12] 6c	Si:[0.53,0.53,0.33], [0,0.47,0.67], [0.47,0,0]

Table 7-3. Crystal structure and crystallographic information of α-SiO_2

At the top – VESTA image of quartz stucture[20]. At the bottom – Crystallographic information: Crystal system, lattice parameters, space group, point group, unit cell, ADPs and position of atoms[45]

The first steps (Building the unit cell, Creating list of lattice planes, Transforming the unit cell, Calculating cleaving abilities) were executed in the same manner as for the Si structure. In this case there were two types of atoms, so the ADPs were calculated for each one of them, using equations 5.6-5.7. At the final step a stereographic projection of the reciprocal directions of quartz reciprocal lattice was plotted, as shown in Figure 7.3. The minimum interplanar distance was set as d_{min} = 1Å. Lattice planes with high CA values are summed up in Table 7-4, as well as the cleavage energies of these planes.

Lattice plane	{011}	{101}	{112}	{010}	{110}	{001}	{111}
CA [$Å^3/e$]	3.06	2.95	1.87	1.83	1.66	1.61	1.52
$\Gamma_0[J/m^2]$	9.30	–	–	11.52	8.88	12.28	10.90

Table 7-4. Cleavage energies and CA values of Quartz crystal structure[44]

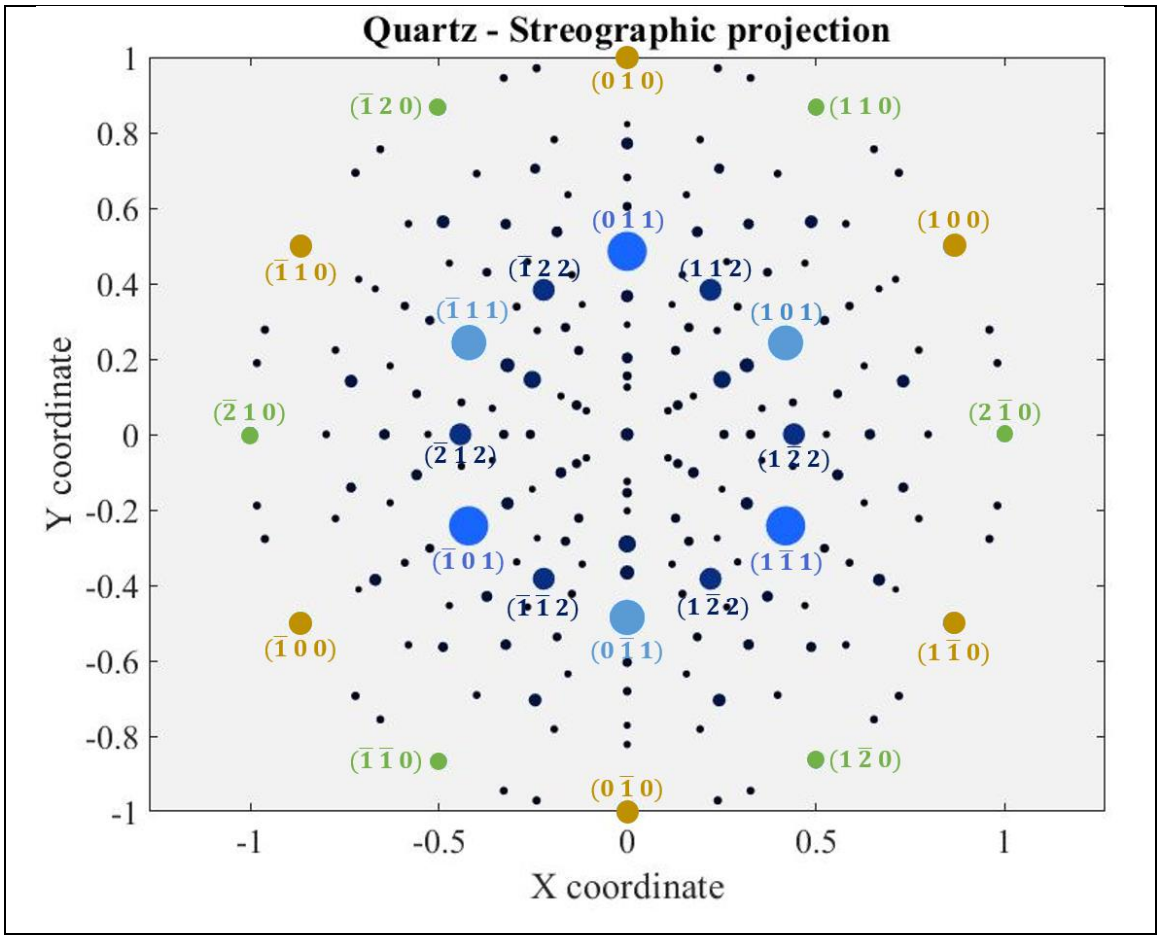

Figure 7.3. Streographic projection of the reciprocal directions of quartz reciprocal lattice; Each point represents a reciprocal direction which is normal to a quartz lattice plane

Figure 7.4 visualizes how our algorithm works on planes (011) and (110). The maximum CA value for plane (011) is 3.06 [$Å^3/e$] and it is obtained for section z* = 0.5 (parallel to [010] direction), as can be seen on Figure 7.4a. We can see three different sections (z* = 0, 0.5, 1) of average atomic density plots in Figure 7.4b, for minimum and maximum CA values. For the (110) plane, the CA value is 1.68 [$Å^3/e$], and it was obtained for section z* = 0.16 (parallel to [-110] directions, as shown in **Error! Reference source not found.**c. The average atomic density plots for sections z* = 0.16 and z* = 0.5 are displayed on Figure 7.4d.

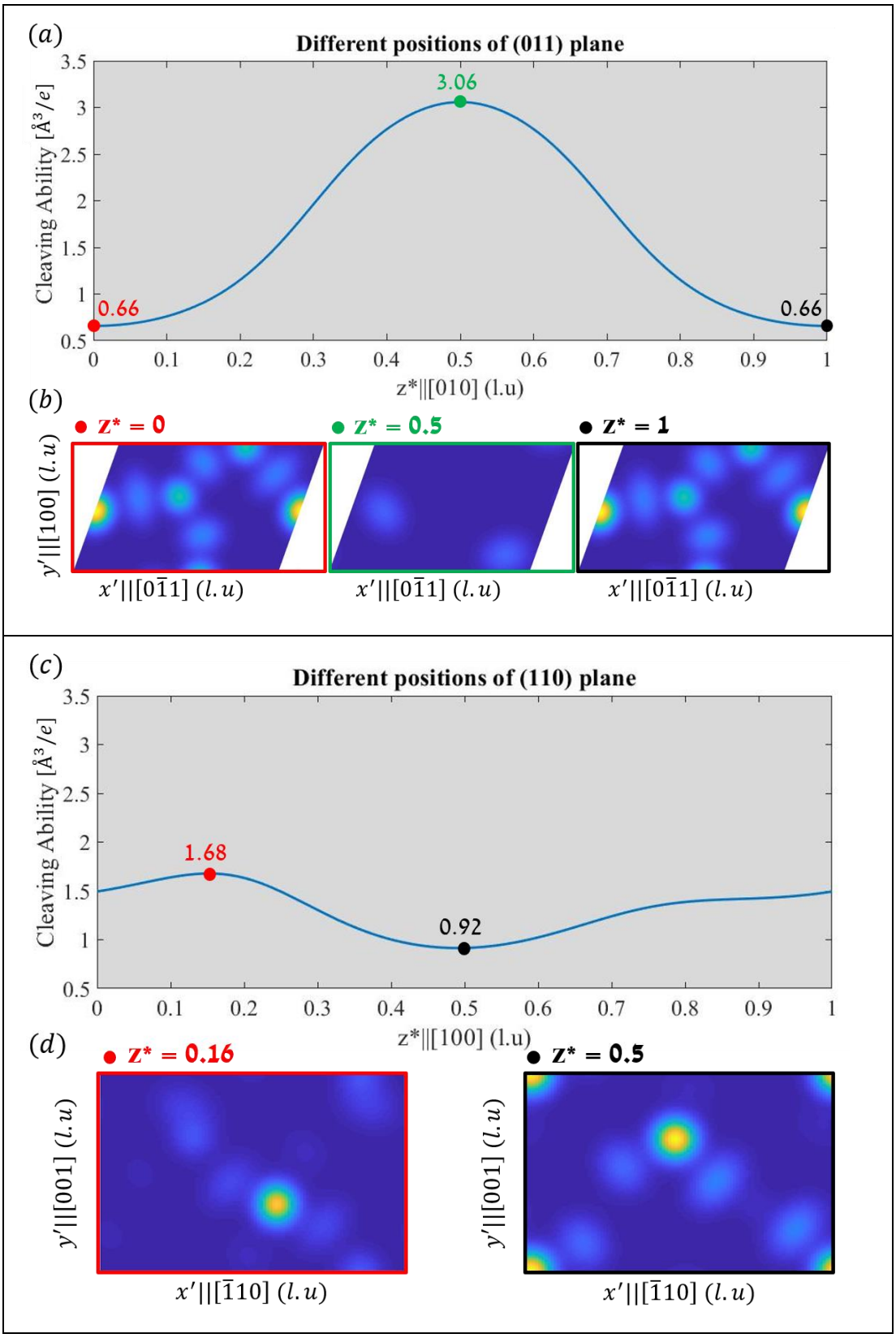

Figure 7.4. CA values and different sections of (011) and (110) planes of quartz crystal structure; (a) Cleaving ability of plane (011) vs z* coordinate (||[010]). (b) Images of different sections of (011) plane along z*. (c) Cleaving ability of plane (110) vs z* coordinate (||[100]). (d) Images of different sections of (110) plane along z*.

7.3 Lithium Niobate

The third crystal structure was Lithium Niobate ($LiNbO_3$), which is one of the most used and investigated crystalline dielectric materials at the present days[46–50]. $LiNbO_3$ presents a very interesting combination of properties that enables to tailor its behavior for many useful devices[51–56]. In the unit cell there are 6 lithium atoms, 6 niobium atoms, and 18 oxygen atoms. The Li as well as the Nb atoms has six nearest neighbors (oxygen atoms). $LiNbO_3$ structure has three known cleavage planes (100), (012) and $(\bar{2}16)$. The first two has cleavage energies of 1.3 and $2.2\,J/m^2$, and the third has a cleavage energy lower than $1.3\,J/m^2$ respectively[12].

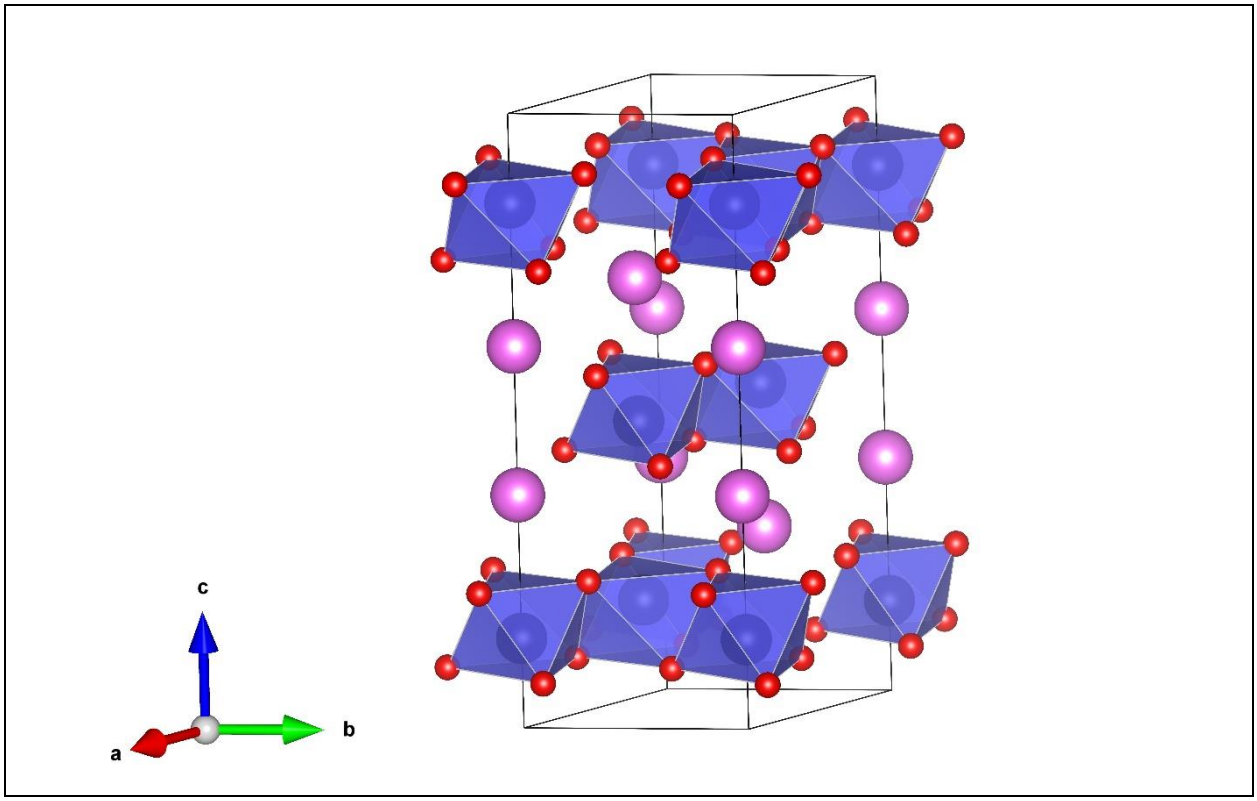

Crystal system: Trigonal Lattice parameters (hexagonal setting): $a_1 = a_2 = 5.15Å \ a_3 = 13.86Å$ $\alpha = \beta = 90^0 \ \gamma = 120^0$ Space group: $R3c$ (161) Point group: $3m$ Unit cell: Li [0, 0, 0.28] 6a Nb [0, 0, 0.99] 6a O [0.05, 0.34, 0.06] 18b Atomic displacement parameters: Li [0.01, 0.01, 0.02, 0, 0, 0.006]	Nb [0.005, 0.005, 0.004, 0, 0, 0.002] O [0.007, 0.006, 0.007, -0.002, -0.001, 0.003] Position of atoms (fractional coordinates): Li: [0,0,0.28], [0,0,0.78], [0.33,0.67,0.45], [0.33,0.67,0.95], [0.67,0.33,0.11], [0.67,0.33,0.61] Nb:[0,0,0], [0,0,0.5], [0.33,0.67,0.17], [0.33,0.67,0.67] [0.67,0.33,0.33], [0.67,0.33,0.83] O: [0.32,0.04,0.40], [0.66,0.70,0.06], [0.99,0.37,0.73], [0.05,0.70,0.56], [0.38,0.37,0.23], [0.71,0.04,0.90], [0.30,0.95,0.06], [0.63,0.62,0.73], [0.96,0.29,0.40], [0.32,0.29,0.90], [0.66,0.95,0.56], [0.99,0.62,0.23], [0.30,0.34,0.56], [0.63,0.01,0.23], [0.96,0.68,0.90], [0.05,0.34,0.06], [0.38,0.01,0.73], [0.71,0.68,0.40]

Table 7-5. Crystal structure and crystallographic information of $LiNbO_3$;
At the top – VESTA image of lithium niobate stucture[20]. At the bottom – Crystallographic information: Crystal system, lattice parameters, space group, point group, unit cell, ADPs and position of atoms[57]

The first steps were executed in the same manner as for the Si structure. In this case there were three types of atoms, so the ADPs were calculated for each one of them. Stereographic projection was plotted in the same manner as for silicon and quartz, as shown in Figure 7.5. The minimum interplanar distance was set as d_{min} = 1.5Å. Lattice planes with high CA values as well as cleavage energies are displayed in Table 7-6. Plane (116) is symmetry equivalent to $(\bar{2}16)$ who was introduced above.

Lattice plane	{012}	{104}	{100}	{110}	{116}
CA $[Å^3/e]$	2.95	2.16	2.09	2.06	1.89
$\Gamma_0[J/m^2]$	2.2	–	1.3	–	<1.3

Table 7-6. Cleavage energies and CA values of LiNbO3 crystal structure[12]

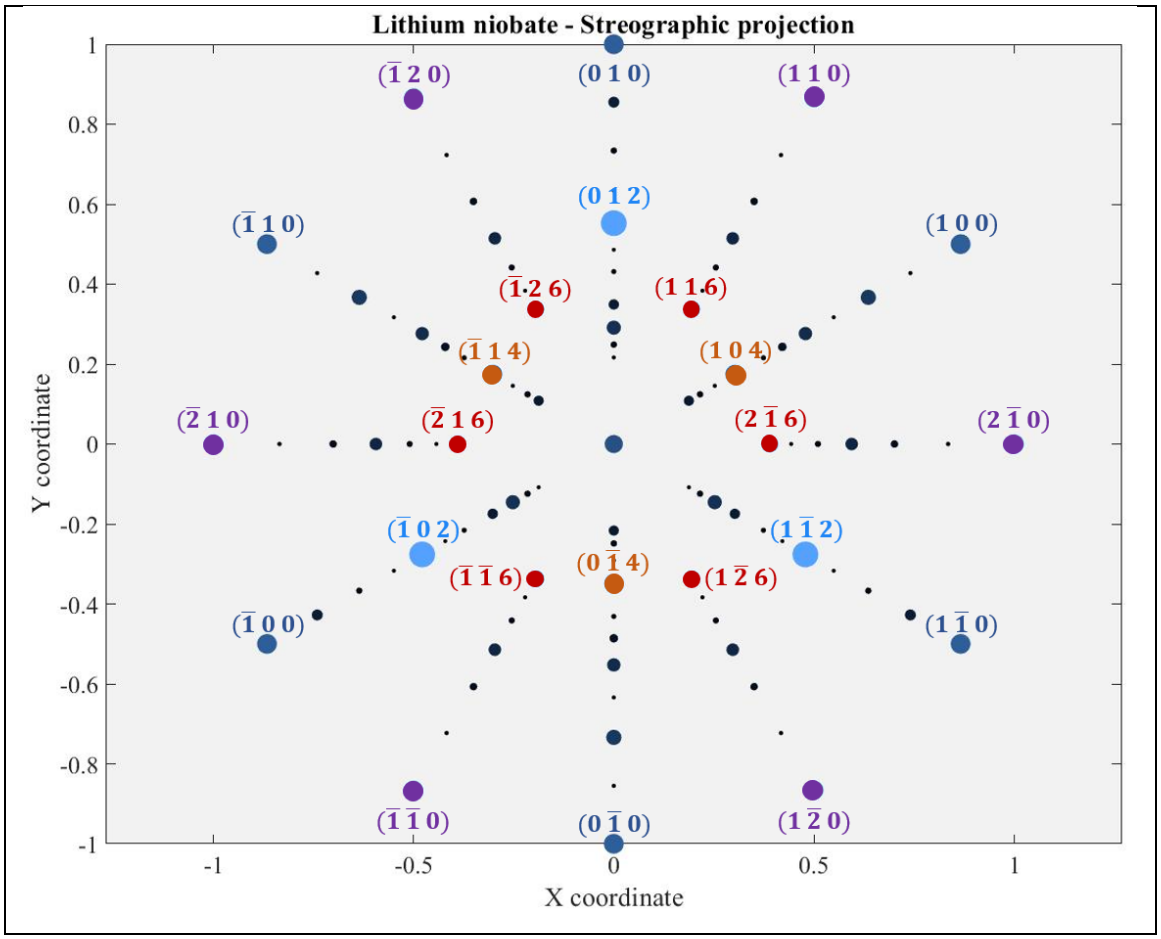

Figure 7.5. Streographic projection of the reciprocal directions of lithium niobate reciprocal lattice; Each point represents a reciprocal direction which is normal to a lithium niobate lattice plane

In Figure 7.6 the algorithm is visualized on planes (012) and (116). The maximum CA value for plane (012) is 2.95 [$Å^3/e$] and it is obtained for section z* = 0.8 (parallel to [0-11] direction), as can be seen on Figure 7.6a. Its corresponding average atomic density plot is displayed in Figure 7.6b together with the plots for sections z* = 0 and z* = 0.56 with CA values of 0.17 and 0.90 [$Å^3/e$] respectively. For the (116) plane, the maximum CA value is 1.89 [$Å^3/e$] and it is obtained for section z* = 0.36 (parallel to [-501] direction), as can be seen on **Error! Reference source not found.**c. The average atomic density plots of this section together with z* = 0.01 and z* = 0.99 is displayed on Figure 7.6d.

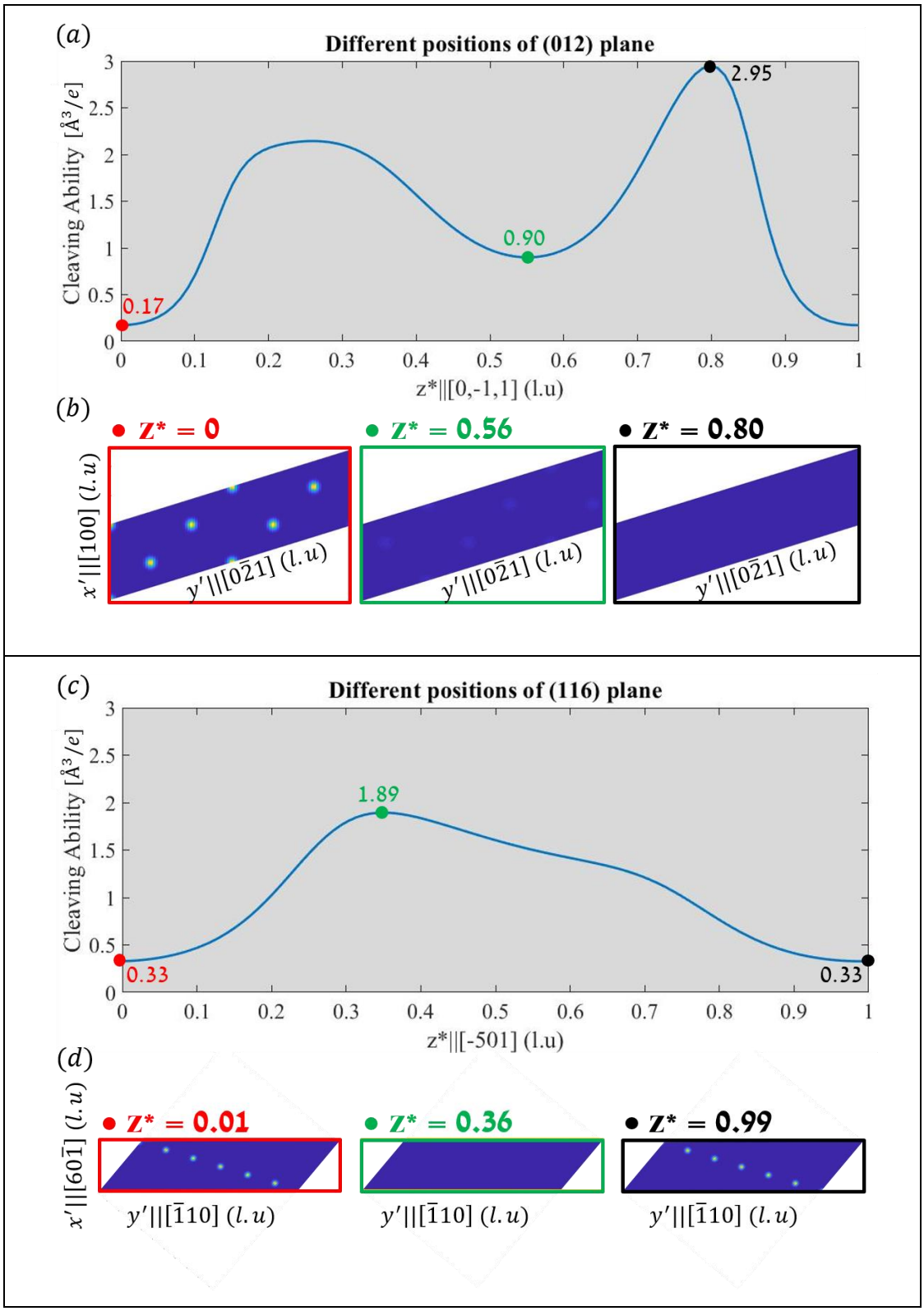

Figure 7.6. CA values and different sections of (011) and (110) planes of $LiNbO_3$ crystal structure; (a) Cleaving ability of plane (012) vs z* coordinate (||[0-11]). (b) Images of different sections of (012) plane along z*. (c) Cleaving ability of plane (116) vs z* coordinate (||[-501]). (d) Images of different sections of (116) plane along z*.

8 Discussion

8.1 Silicon

Silicon has the simplest crystal structure out of the three, and this is why we chose to start with it. For our purpose it served us pretty much as a reference. Silicon has only two cleavage planes (110) and (111) with cleavage energies 3.46 and $2.88\,[J/m^2]$, respectively. While the CA values ranged between $1.43 - 55.77\,[\text{Å}^3/e]$, the CA calculated for (110) and (111) were 8.99 and $55.77\,[\text{Å}^3/e]$, respectively. We can confidently say that our model predicted these two cleavage planes, and even in the "right order". Meaning that for (111) plane the CA was greater than for (110) plane, what makes sense because the CE of (111) plane is lower than that of (110) plane.

We can also notice that the CA of (111) plane was ~7 times bigger than that of (110) plane. That may mistakenly lead us to the intuition that (111) plane will tend to cleave way more easily than (110) plane. Looking again at the cleavage energies of these planes we see that the difference between them is less than 20%. Beyond the fact that CA and CE have different units and shouldn't be compared, they are also conceptually different. Where CE is mostly related to the number of bonds (and its strength) per unit area, CA calculation is in fact a program substitutes the manual inspection process, searching for the least dense plane (highest CA value). High CA values can be related to a "geometrical cleavage" rather than the original definition of cleavage, since no bonds are treated. This is the time to mention that the main limitation of the model was that atomic bonds were not treated. Now it's quite clear that CA and CE are two different entities and that a quantitative comparison between them is useless.

8.2 Quartz

For the quartz crystal structure, the CA values were much closer to each other, ranging between $1.27 - 3.06\,[\text{Å}^3/e]$. The median CA calculated was $1.36\,[\text{Å}^3/e]$ and all the cleavage planes displayed in Table 7-4 had significantly greater CA values than the median. Meaning that using the model we have managed to mark the cleavage planes assigning to them relatively high CA values.

On the other hand, while the CA values in Table 7-4 are displayed in a descending order, we might have expected that the cleavage energies will be in an ascending order. As we can see from the table, the CE values may be ordered in an increasing fashion, but the trend is not clear. Furthermore, some of the planes had relatively high CA values but still, they were not recognized as cleavage plane (Table 7-4 includes just a partial list of the planes). Deeper understanding can only be achieved analyzing from a different point of view, treating the atomic bonds in the crystal, but this is out of the scope of this work.

8.3 Lithium Niobate

For the lithium niobate crystal structure, the CA values were also close to each other, in a similar way as for the quartz crystal structure, ranging between $0.77 - 2.95\ [Å^3/e]$. The median CA was $0.96\ [Å^3/e]$, and all three cleavage planes in Table 7-6 had significantly greater CA values. Planes (012) and (100) are well known cleavage planes of lithium niobate, but plane (116) was confirmed experimentally only on July 2020 by Hirsh et al[12]. The fact that our model succeeded predicting these three planes as cleavage planes, especially (116), is of a great importance to us and confirms the validity of our model.

Nevertheless, we can see on Table 7-6 that the CE values is in a descending order, and that some of the planes have high CA values, but they are not cleavage planes. The considerations we introduced for the silicon and quartz crystal structures are still hold for this case. Where CA parameter takes into account only the plane and the section having the lowest average atomic density, cleavage energy involves chemical bonds considerations.

9 Conclusions

We created a model to predict cleavage planes in crystal structures and the model was applied on Si, α-SiO_2 and $LiNbO_3$. For silicon crystal structure the prediction was great, finding its cleavage planes, in the right order. For the α-SiO_2 and $LiNbO_3$ crystal structures our model predicted all the cleavage planes including a relatively new cleavage plane (116) of $LiNbO_3$, assigning to them high CA values. The order of the CA values was partially matching the corresponding cleavage energies, and some additional lattice planes was recognized as potential cleavage planes having high CA values, but in fact they are not

cleavage planes. These results were explained with the lack of treatment of atomic bonds in our model.

For even more accurate predictions, atomic bonds are vital to this model, as the bridge between the geometrical cleavage which our model predicted, and the original cleavage definition.

References

1. Gilman, J. J. Direct Measurements of the Surface Energies of Crystals. J. Appl. Phys. 31, 2208–2218 (1960).
2. Gleizer, A. & Sherman, D. The cleavage energy at initiation of (110) silicon. Int. J. Fract. 187, 1–14 (2014).
3. Pérez, R. & Gumbsch, P. Directional Anisotropy in the Cleavage Fracture of Silicon. Phys. Rev. Lett. 84, 5347–5350 (2000).
4. Hauch, J. A., Holland, D., Marder, M. P. & Swinney, H. L. Dynamic Fracture in Single Crystal Silicon. Phys. Rev. Lett. 82, 3823–3826 (1999).
5. Sankey, O. F. & Niklewski, D. J. Ab initio multicenter tight-binding model for molecular-dynamics simulations and other applications in covalent systems. Phys. Rev. B 40, 3979–3995 (1989).
6. Spence, J. C. H., Huang, Y. M. & Sankey, O. Lattice trapping and surface reconstruction for silicon cleavage on (111). Ab-initio quantum molecular dynamics calculations. Acta Metall. Mater. 41, 2815–2824 (1993).
7. Payne, M. C., Teter, M. P., Allan, D. C., Arias, T. A. & Joannopoulos, J. D. Iterative minimization techniques for ab initio total-energy calculations: molecular dynamics and conjugate gradients. Rev. Mod. Phys. 64, 1045–1097 (1992).
8. Gumbsch, P. An atomistic study of brittle fracture: Toward explicit failure criteria from atomistic modeling. Journal of materials research 10, 2897–2907 (1995).
9. Shenderova, O. A., Brenner, D. W., Omeltchenko, A., Su, X. & Yang, L. H. Atomistic modeling of the fracture of polycrystalline diamond. Phys. Rev. B 61, 3877–3888 (2000).
10. Belytschko, T., Xiao, S. P., Schatz, G. C. & Ruoff, R. S. Atomistic simulations of nanotube fracture. Phys. Rev. B 65, 235430 (2002).
11. Liu, F., Ming, P. & Li, J. Ab initio calculation of ideal strength and phonon instability of graphene under tension. Phys. Rev. B 76, 064120 (2007).
12. Hirsh, Y., Gorfman, S. & Sherman, D. Cleavage and surface energies of LiNbO3. Acta Mater. 193, 338–349 (2020).
13. Danzer, R., Lube, T., Supancic, P. & Damani, R. Fracture of Ceramics. Adv. Eng. Mater. 10, 275–298 (2008).

14. Gumbsch, P., Fischmeister, H. & Kohlhoff, S. Crack propagation in b.c.c. crystals studied with a combined finite-element and atomistic model. Philosophical magazine 64, 851–878 (1991).

15. Telling, R. H., Pickard, C. J., Payne, M. C. & Field, J. E. Theoretical Strength and Cleavage of Diamond. Phys. Rev. Lett. 84, 5160–5163 (2000).

16. Inglis, C. E. Stresses in a Plate due to the Presence of Cracks and Sharp Corners. 53, 219–241.

17. Griffith, A. A. The Phenomena of Rupture and Flow in Solids. R. Aircr. Establ. 221, 587–623 (1920).

18. Lawn, B. Fracture of Brittle Solids. (Cambridge University Press, 1993).

19. Klein, C. & Hurlbut, C. S. Manual of Mineralogy. (John Wiley & Sons, 1985).

20. Momma, K. & Izumi, F. VESTA 3 for three-dimensional visualization of crystal, volumetric and morphology data. Journal of Applied Crystallography 44, 1272–1276 (2011).

21. Graef, M. D. & McHenry, M. E. Structure of materials : an introduction to crystallography, diffraction, and symmetry. (Cambridge University Press, 2012).

22. Poubanne, P., Cailletaud, G. & Me´ric, L. Single Crystal Modeling for Structural Calculations: Part 1—Model Presentation. Journal of engineering materials and technology 113, 162–170 (1991).

23. Park, S.-E. E. & Hackenberger, W. High performance single crystal piezoelectrics: applications and issues. Curr. Opin. Solid State Mater. Sci. 6, 11–18 (2002).

24. Chen, G. et al. Polysynthetic twinned TiAl single crystals for high-temperature applications. Nat. Mater. 15, 876–881 (2016).

25. Caron, P. & Khan, T. Evolution of Ni-based superalloys for single crystal gas turbine blade applications. Aerosp. Sci. Technol. 3, 513–523 (1999).

26. Sun, E. & Cao, W. Relaxor-based ferroelectric single crystals: Growth, domain engineering, characterization and applications. Prog. Mater. Sci. 65, 124–210 (2014).

27. Feng, X. et al. Vertically Aligned Single Crystal TiO_2 Nanowire Arrays Grown Directly on Transparent Conducting Oxide Coated Glass: Synthesis Details and Applications. Nano Lett. 8, 3781–3786 (2008).

28. Coppens, P. Title: X-Ray Charge Densities and Chemical Bonding. (Oxford University Press, 1997).

29. Chen, R. & Trucano, P. Structure of graphite by neutron diffraction. Nature 258, 136–137 (1975).

30. Bernstein, N. & Hess, D. W. Lattice Trapping Barriers to Brittle Fracture. Phys. Rev. Lett. 91, 025501 (2003).

31. Brede, M. & Haasen, P. The brittle-to-ductile transition in doped silicon as a model substance. Acta Metall. 36, 2003–2018 (1988).

32. Bouchard, P.-O., Roberto, M., Bernacki, M. & Masolin, A. Thermo-mechanical and fracture properties in single-crystal silicon. Journal of materials science 48, 979–988 (2013).

33. Kleiman, R. N., Agnolet, G. & Bishop, D. J. Two-level systems observed in the mechanical properties of single-crystal silicon at low temperatures. Phys. Rev. Lett. 59, 2079–2082 (1987).

34. Hom, T., Kiszenik, W. & Post, B. Accurate lattice constants from multiple reflection measurements. II. Lattice constants of germanium silicon, and diamond. J. Appl. Crystallogr. 8, 457–458 (1975).

35. Wilshaw, T. & Hartley, N. E. Deformation and Fracture of Synthetic alpha Quartz. Journal of materials science 8, 265–278 (1973).

36. Griggs, D. Hydrolytic Weakening of Quartz and Other Silicates*. Geophys. J. R. Astron. Soc. 14, 19–31 (2010).

37. Parks, G. A. Surface and interfacial free energies of quartz. J. Geophys. Res. Solid Earth 89, 3997–4008 (1984).

38. Payne, B. & Ball, A. The tensile fracture of quartz crystals. Journal of materials science 11, 731–740 (1976).

39. Weil, J. A. A review of electron spin spectroscopy and its application to the study of paramagnetic defects in crystalline quartz. Phys. Chem. Miner. 10, 149–165 (1984).

40. O'Sullivan, C. K. & Guilbault, G. G. Commercial quartz crystal microbalances – theory and applications. Biosens. Bioelectron. 14, 663–670 (1999).

41. Shou-Zhuo, Y. & Zhi-Hong, M. Frequency properties of a piezoelectric quartz crystal in solutions and application to total salt determination. Anal. Chim. Acta 193, 97–105 (1987).

42. Sterner, S. M. & Bodnar, R. J. Synthetic fluid inclusions in natural quartz I. Compositional types synthesized and applications to experimental geochemistry. Geochim. Cosmochim. Acta 48, 2659–2668 (1984).

43. Martin, R. J. Time-dependent crack growth in quartz and its application to the creep of rocks. J. Geophys. Res. 77, 1406–1419 (1972).

44. Iwasa, M. & Bradt, R. C. Cleavage of Natural and Synthetic Single Crystal Quartz. Mat. Res. Bull 22, 1241–1248 (1987).

45. Levien, L., Prewitt, C. T. & Weidner, D. J. Structure and elastic properties of quartz at pressure. Am. Mineral. 65, 920–930 (1980).

46. Arizmendi, L. Photonic applications of lithium niobate crystals. Phys. Status Solidi A 201, 253–283 (2004).

47. Marsh, P. & Abrahams, S. C. Defect structure dependence on composition in lithium niobate. Acta crystallographica 42, 61–68 (1986).

48. Reddy, J. M. & Bernstein, J. L. Ferroelectric Lithium Niobate Single Crystal X-ray Diffraction Study at 24°C.

49. Weis, R. S. & Gaylord, T. K. Lithium niobate: Summary of physical properties and crystal structure. Appl. Phys. Solids Surf. 37, 191–203 (1985).

50. Gruber, M. et al. Strength distribution and fracture analyses of $LiNbO_3$ and $LiTaO_3$ single crystals under biaxial loading. J. Eur. Ceram. Soc. 37, 4397–4406 (2017).

51. Ulliac, G., Calero, V., Ndao, A., Baida, F. I. & Bernal, M.-P. Argon plasma inductively coupled plasma reactive ion etching study for smooth sidewall thin film lithium niobate waveguide application. Opt. Mater. 53, 1–5 (2016).

52. Shah, R. R., Kim, D. M., Rabson, T. A. & Tittel, F. K. Characterization of iron-doped lithium niobate for holographic storage applications. J. Appl. Phys. 47, 5421–5431 (1976).

53. Hukriede, J., Runde, D. & Kip, D. Fabrication and application of holographic Bragg gratings in lithium niobate channel waveguides. J. Phys. Appl. Phys. 36, R1–R16 (2003).

54. Binh, L. N. Lithium niobate optical modulators: Devices and applications. J. Cryst. Growth 288, 180–187 (2006).

55. Ghione, G. et al. Microwave modeling and characterization of thick coplanar waveguides on oxide-coated lithium niobate substrates for electrooptical applications. IEEE Trans. Microw. Theory Tech. 47, 2287–2293 (1999).

56. Shur, V. Ya. et al. Regular ferroelectric domain array in lithium niobate crystals for nonlinear optic applications. Ferroelectrics 236, 129–144 (2000).

57. Hsu, R., Maslen, E. N., Du Boulay, D. & Ishizawa, N. Synchrotron X-ray studies of $LiNbO_3$ and $LiTaO_3$. Acta Crystallogr. B 53, 420–428 (1997).

תקציר

ביקוע מתאר את הנטייה של גביש להישבר בקלות לאורך מישורים קריסטלוגרפיים. רכישת הידע אודות ביקוע עבור מיקרומבנה של גביש נתון הינו הכרחי הבנה ומחקר של תכונות מכאניות בולטות כמו חסינות לשבר, משיכות וחוזק. למרות שמישורי ביקוע בדרך כלל ידועים עבור חומרים פשוטים (למשל מישורים (110) ו – (111) עבור סיליקון), המידע הזה אינו זמין עבור גבישים רבים.

כיום לא ידוע על שיטות חישוביות פשוטות לחיזוי מישורי ביקוע בגביש יחיד, מלבד בדיקה ויזואלית של מבנים תלת-ממדיים בעזרת תוכנות גרפיות כמו CrystalMaker או VESTA. פיתוח שיטה כזו יכול לתרום משמעותית להבנה של תכונות פיזיקליות ומכניות של גבישים. בנוסף, שיטה כזו יכולה לחזות מישורי ביקוע קיימים ולחזות מישורים שעוד לא אושרו ניסיונית.

מטרתה של עבודה זו היא לפתח אלגוריתם ותוכנת מחשב לבדיקה אוטומטית של מבנים גבישיים וחיזוי מועמדים מרכזיים להיות מישורי ביקוע. האלגוריתם ממספר את כל המישורים האפשריים, משייך מצייני מילר לכל מישור, סופר את מספר האטומים החותכים כל מישור והמיקום שלהם עבור כיוון קריסטלוגרפי נתון. מידלנו את האטומים בעזרת אליפסואידים תרמיים – פונקציית צפיפות הסתברות (PDFs) אשר נובעים ממקדמי ההעתקה האטומיים (ADPs). האלגוריתם נבדק על שלושה מבני גביש אנאורגניים פשוטים – סיליקון, קוורץ וליתיום ניובאט.

אנו מאמינים שהאלגוריתם שלנו יכול לשמש לחיזוי מהיר, יעיל ואינטואיטיבי של מישורי ביקוע, אשר לאחר מכן יאושרו בצורה קפדנית ואיטית יותר על ידי חישובי DFT.

אוניברסיטת תל אביב
הפקולטה להנדסה ע״ש איבי ואלדר פליישמן
בית הספר לתארים מתקדמים ע״ש זנדמן-סליינר

אלגוריתם אוניברסלי לחיזוי מישורי ביקוע בגביש יחיד

חיבור זה הוגש כעבודת גמר לקראת התואר ״מוסמך אוניברסיטה״
במדע והנדסה של חומרים
על – ידי

אוריאל ווקנין

העבודה נעשתה במחלקה למדע והנדסת חומרים ובבית הספר להנדסה
מכנית בהנחייתם של ד״ר סמיון גורפמן ופרופ׳ דב שרמן

אלול התש״פ

אלגוריתם אוניברסלי לחיזוי מישורי ביקוע בגביש יחיד

חיבור זה הוגש כעבודת גמר לקראת התואר "מוסמך אוניברסיטה"
במדע והנדסה של חומרים
על – ידי

אוריאל ווקנין

אלול התש"פ
